

Surface Preparation of Polymer Composites Embedded Metal Mesh for Coating Using Optimized Grit-Blasting Process and Image Analysis

Pooria Sedigh Rahimabadi

A Thesis

In the Department

of

Mechanical Industrial and Aerospace Engineering

Presented in Partial Fulfillment of the Requirements

for the Degree of

Master of Applied Science (Mechanical Engineering)

at Concordia University

Montreal, Quebec, Canada

August 2022

© Pooria Sedigh Rahimabadi, 2022

CONCORDIA UNIVERSITY
School of Graduate Studies

This is to certify that the thesis prepared

By: Pooria Sedigh Rahimabadi

Entitled: Surface Preparation of Polymer Composites Embedded Metal Mesh for Coating
Using Optimized Grit-Blasting Process and Image Analysis

and submitted in partial fulfillment of the requirements for the degree of

Master of Applied Science

in

Mechanical Engineering

complies with the regulations of the university and meets the accepted standards with respect to
originality and quality.

Signed by the final Examining Committee:

Chair

Dr. Tsz Ho Kwok

Internal Examiner

Dr. Tsz Ho Kwok

External Examiner

Dr. Ahmed Soliman

Supervisor

Dr. Mehdi Hojjati

Approved by: Chair of Department or Graduate Program Director

Martin Pugh

Dean, Gina Cody School of Engineering and Computer Science

Mourad Debbabi

ABSTRACT

Surface Preparation of Polymer Composites Embedded Metal Mesh for Coating Using Optimized Grit-Blasting Process and Image Analysis

Pooria Sedigh Rahimabadi

Many advantages of fiber reinforced polymer composites (FRPCs) make them suitable for various industrial applications, especially aerospace. However, they possess limitations, such as low thermal and electrical conductivity, as well as relatively low erosion resistance. This has led to in-service failure of FRPCs causing fatal accidents, as well as the waste of materials and equipment. In order to overcome these limitations, surface coating and metallization of FRPCs is a potential resolution. For this purpose, the incorporation of a metal wire mesh in the outermost layer of the composites forms a superficial anchor for the deposition of metals using thermal sprays, which has been proven to be an effective method. However, obtaining a proper surface coating is yet dependent on the mesh exposure level of the fully resin-covered metal mesh by surface preparation methods before the coating process. In this study, optimization of grit blasting parameters and introduction of operational parameter maps for preventing damage to the mesh pattern and composite during grit-blasting are carried out. An in-house automated sample holder for grit blasting process is designed and assembled allowing for better control over the grit blasting process. Then, the effect of grit blasting pressure, time, and stand-off distance at three levels on the exposure level of metal mesh were investigated through systematic experimentation. Portable digital microscopy and conventional optical microscopy are employed to inspect the composite surface and to measure the level of polymer removal at each processing condition. According to the results, it is practical to achieve a desirable metal mesh exposure following the optimized grit-blasting parameters. Moreover, developing a computer-aided inspection system can enormously contribute to the realization of uniform, and efficient grit blasting in industrial applications for huge structural parts.

Keywords: Carbon fiber-reinforced polymer composite; Grit-blasting; Coatability.

Acknowledgments

I would like to express my gratitude and appreciation for my esteemed supervisor, Prof. Mehdi Hojjati, whose guidance, support, and encouragement have been invaluable throughout my M.A.Sc program. Beyond doubt, it was not possible to carry out this project without his supervision, insights, and tutelage.

It is also a pleasure to express my special thanks to all my friends in composites and thermal spray groups, and the Concordia research staff, especially, Dr. Daniel Rosca, Dr. Ali Akbar Nozari, and Saeed Garmeh. I deeply appreciate their mentorship, helpfulness, and willingness in providing useful information and training for this study.

Lastly, I wish to express my sincere gratitude to my family for their encouragement and moral support.

Table of Content

List of Figures	vii
List of Tables	x
CHAPTER 1:INTRODUCTION	1
1.1. Polymer Composites	2
1.2. Coating and Surface Metallization of FRPCs	3
1.3. Surface Preparation Prior to Coating	5
1.4. Aims and Objectives	6
1.5. Thesis Outline	7
CHAPTER 2:LITERATURE REVIEW	9
2.1. Fiber Reinforced Polymer Composites (FRPCs)	10
2.1.1. Fibers	10
2.1.2. Polymer Matrices	12
2.1.2.1. Thermosetting	12
2.1.2.1.1. Epoxies	13
2.1.2.1.2. Polyesters	14
2.1.2.1.3. Vinyl Esters	15
2.1.2.1.4. Polyurethane Resins	15
2.1.2.1.5. Bismaleimide Resins	16
2.1.2.2. Thermoplastic	16
2.2. Coating methods for FRPCs	17
2.2.1. Thermal Sprays	17
2.2.1.1. Flame Spray	18
2.2.1.2. Wire Arc Spray	19
2.2.1.3. Plasma Spray	19
2.2.1.4. High-Velocity Air/Oxygen Fuel (HVOF/HVOF)	21
2.2.1.5. Cold Spray	21
2.2.2. Electroless Deposition	22
2.2.3. Chemical Vapor Deposition (CVD)	22
2.2.4. Physical Vapor Deposition (PVD)	23
2.3. Grit-blasting	23
CHAPTER 3:EXPERIMENTAL AND ANALYTICAL METHODOLOGY	26
3.1. Fabrication of Metal Mesh Incorporated FRPC	27

3.2.	Sandpaper Polishing	31
3.3.	Grit-Blasting Process	32
3.4.	Automated Grit-Blasting Setup	35
3.4.1.	Design and Assembly	35
3.4.2.	Programming & Features	40
3.4.2.1.	Code Setup	40
3.4.2.2.	Input	41
3.4.2.3.	Computation and Output	42
3.4.3.	Protection and Safety	42
3.4.4.	Design of Experiment	44
3.5.	Characterization	47
3.5.1.	Portable Digital Microscopy	47
3.5.2.	Optical Microscopy	48
3.5.3.	Roughness Measurement	50
CHAPTER 4: RESULTS AND DISCUSSION		52
4.1.	The Effect of Sandpaper polishing	53
4.2.	The Effect of Grit-blasting	55
4.2.1.	Visual Inspection	55
4.2.2.	Digital Microscopy Inspection	59
4.2.3.	Validation through Optical Microscopy	65
4.2.4.	Regression Analysis	68
4.2.5.	Operation Window Map	71
4.2.6.	Optimization of Parameters	74
4.2.7.	Effective Radius of the Gun	75
4.2.8.	Surface Roughness	77
4.2.9.	Effect of Grits	78
CHAPTER 5: CONCLUSION AND FUTURE WORK		79
5.1.	Conclusion	80
5.2.	Future Work	82
REFERENCES		84

List of Figures

Figure 1.1. A schematic representation of preparing FRPC for thermal spray coating by incorporation of superficial metal mesh in the system and grit-blasting.	5
Figure 2.1. Scanning electron microscope image of a developed surface coating on garnet sand roughened FRPC sample [89].	18
Figure 2.2. Cross-section of a coated metal mesh/ FRPC substrate using plasma spray [51].	20
Figure 2.3. Schematics of a) suction blasting and b) pressure blasting equipment [137].	25
Figure 3.1. Digital microscope image of 316 stainless steel metal mesh 200.	27
Figure 3.2. A schematic representation of vacuum bagging setup of metal mesh/FRPC.	29
Figure 3.3. The applied heat cycle and pressure on the system during the curing stage in the autoclave. .	30
Figure 3.4. Images of As-fabricated metal mesh/CFRP plates, a) showing a perfectly manufactured plate, while b) demonstrate lack of complete coverage of metal mesh by resin due to strong suction effect of vacuum.	30
Figure 3.5. A designed and robotic polishing machine [138].	32
Figure 3.6. Schematic of ECO-420 sandblasting cabinet for light-duty application along with its main components.	34
Figure 3.7. Perspective schematic views of the initial designed setup for automated grit-blasting.	36
Figure 3.8. The employed linear stage actuators equipped with NEMA23 Stepper motors for the automated setup.	36
Figure 3.9. The pattern of grit-blasting and movement of the stage in front of the grit-blasting gun as a loop starting with the left image.	38
Figure 3.10. A schematic of the wiring of each stepper motor to its TB6600 driver and Arduino Uno kit.	39
Figure 3.11. A schematic of the wiring of the LCD and IR remote control receiver to the Arduino Uno kit.	39
Figure 3.12. A view of the assembled automated grit-blasting setup.	40
Figure 3.13. a) a schematic of the cross-section of resin-covered metal mesh in the metal mesh/CFRP system in the ideal condition revealing the dimensional characteristic and an approximate measure for mesh exposure. b) a top view optical microscope image of sandpaper polished coupon demonstrating exposure of metal wires and its dependency to cross-sectional view.	47

Figure 3.14. A view of the characterization utilizing a portable digital microscope.	48
Figure 3.15. A schematic of an optical light microscope, its components, and working principle [139]...	49
Figure 3.16. An image of the coupons prepared for grit-blasting, sample cut in half, and samples mounted for polishing and characterization by optical microscope.....	50
Figure 3.17. Mitutoyo SJ 210 profilometer.....	51
Figure 4.1. Optical microscope images of polished samples with sandpaper of a) 180, b) 320, c) 600.	53
Figure 4.2. Images of samples 1-9 (grit-blasted under the pressure of 60 psi) in comparison to the as-fabricated state utilized for visual inspection.....	56
Figure 4.3. Images of samples 10-18 (grit-blasted under the pressure of 80 psi) in comparison to the as-fabricated state utilized for visual inspection.	57
Figure 4.4. Images of samples 19-27 (grit-blasted under the pressure of 100 psi) in comparison to the as-fabricated state utilized for visual inspection.	58
Figure 4.5. Digital microscope images of samples 1-3 (grit-blasted under P=60 psi with d= 7cm), along with their corresponding distribution of metal wire exposure length.....	59
Figure 4.6. Digital microscope images of samples 4-6 (grit-blasted under P=60 psi with d= 10cm), along with their corresponding distribution of metal wire exposure length.....	60
Figure 4.7. Digital microscope images of samples 7-9 (grit-blasted under P=60 psi with d= 13cm), along with their corresponding distribution of metal wire exposure length.....	60
Figure 4.8. Digital microscope images of samples 10-12 (grit-blasted under P=80 psi with d= 7cm), along with their corresponding distribution of metal wire exposure length.....	61
Figure 4.9. Digital microscope images of samples 13-15 (grit-blasted under P=80 psi with d= 10cm), along with their corresponding distribution of metal wire exposure length.....	61
Figure 4.10. Digital microscope images of samples 16-18 (grit-blasted under P=80 psi with d= 13cm), along with their corresponding distribution of metal wire exposure length.....	62
Figure 4.11. Digital microscope images of samples 19-21 (grit-blasted under P=100 psi with d= 7cm), along with their corresponding distribution of metal wire exposure length.....	62
Figure 4.12. Digital microscope images of samples 22-24 (grit-blasted under P=100 psi with d= 10cm), along with their corresponding distribution of metal wire exposure length.....	63
Figure 4.13. Digital microscope images of samples 25-27 (grit-blasted under P=100 psi with d= 13cm), along with their corresponding distribution of metal wire exposure length.....	63
Figure 4.14. Low magnification optical microscope images of grit-blasted samples showing various states of surface preparation in comparison to as-fabricated state.	66

Figure 4.15. High magnification optical microscope images of grit-blasted samples showing various states of surface preparation in comparison to as-fabricated state.	67
Figure 4.16. Bar plot of mesh exposure level versus grit-blasting parameters (observed and estimated data).	70
Figure 4.17. Plot of residuals for predicted values of mesh exposure level using a) Fit-1, b) Fit-2, and c) Fit-3, from observed/estimated ones.	70
Figure 4.18. 2D surface map of mesh exposure level dependent on P and t, at d = 13 cm.	71
Figure 4.19. 2D surface map of mesh exposure level dependent on P and t, at d = 11 cm.	72
Figure 4.20. 2D surface map of mesh exposure level dependent on P and t, at d = 10 cm.	72
Figure 4.21. 2D surface map of mesh exposure level dependent on P and t, at d = 9 cm.	73
Figure 4.22. 2D surface map of mesh exposure level dependent on P and t, at d = 7 cm.	73
Figure 4.23. Image of a sample grit-blasted at one point under the pressure of 100 psi at various distances demonstrating the four regions of the grit-blasting zone.	76
Figure 4.24. Digital microscope images of the unused and used grits.	78

List of Tables

Table 1.1. Mechanical, thermal, and electrical properties of common engineering materials and FRPCs...	2
Table 1.2. Common surface preparation methods and their effect on metals and polymers [52].....	6
Table 2.1. Properties of commercially available abrasive media for the grit-blasting process [137].	25
Table 3.1. dimensional characteristics of 316 stainless steel metal mesh 200.....	28
Table 3.2. Specifications and dimensions of the ECO-420 sandblasting cabinet.....	34
Table 3.3. The specifications of the linear stage actuators and their stepper motors.....	37
Table 3.4. the parameter sets of design of experiment testing for analysis and optimization of grit-blasting process for metal mesh/CFRP system.....	45
Table 4.1. The mesh exposure level, along with the results predicted by three different regression model and confidence interval of the best fit based on the design of experiment.....	69
Table 4.2. Coefficients for transformed response regression model (Fit-3).	70
Table 4.3. Optimization parameters and solution for enhancing safe window and reducing operation time.	74
Table 4.4. The effective radius of grit-blasting at various pressure and distances.....	76
Table 4.5. Measured surface roughness of the grit-blasted samples.....	77

Chapter 1: Introduction

1.1. Polymer Composites

The development of polymer matrix composites (PMCs), especially fiber reinforced polymer composites (FRPCs), has been a focal point of research in various fields of study during the last decades. This class of engineering materials has found numerous applications in the aeronautical and transportation industries, intelligent materials for civil technological infrastructures, leisure equipment, electronics, maritime, biotechnology, and energy sector [1,2]. This enlarging window of applications has been actualized as a result of significant properties of FRPCs, i.e., brilliant specific strength and stiffness, good fatigue life, and noticeable corrosion resistance [3–6]. In order to provide a better viewpoint, the properties of common FRPCs are summarized in Table 1.1 along with those of other engineering materials. It is worth mentioning that the range of properties reported in Table 1.1 are corresponding to the room temperature condition, and the range of outlined values is dependent on various parameters such as manufacturing method, chemical composition, post thermal, mechanical, and/or chemical treatments.

Table 1.1. Mechanical, thermal, and electrical properties of common engineering materials and FRPCs

Material	ρ (gr/cm³)	E (GPa)	σ_{UTS} (MPa)	ϵ_f (%)	α ($\mu\text{m}/\text{m.K}$)	K_c (W/m.K)	Ref
AISI 316	~8	193	50-590	25-45	15.9	~13	[7–10]
AHSS	7.2-7.8	190-220	400-1900	5-35	-	-	[11,12]
Cast iron	7.2-7.8	90-210	170-700	1-26	10.5-12	32-50	[7]
Al alloys	2.6-2.8	69-79	70-620	9-45	23.0-23.6	121-239	[7,13]
Cu alloys	8.9	112-129	209-344	14-60	16.5	401	[7,14]
Ti-6Al-4V	4.4	115	1000-1175	10-14	9	7	[15]
Al ₂ O ₃	4-4.5	260-410	68-665	0.1	4.5-5.5	15-40	[16,17]
SiC	3.1	240-480	240-1625	~1.8	4.7-5.1	320-490	[18,19]
Wood	0.29-0.78	0.5-28	0.7-7	-	2-60	0.1-0.4	[19,20]
CFRP	1.5-2.1	37-784	600-3900	0.5-1.8	-9.0	0.26-18	[21–23]
GFRP	1.25-2.5	35-86	500-4600	1.2-5.0	6.0-10.0	0.1-0.8	[21,24,25]
AFRP	1.25-1.45	41-175	1700-3600	1.4-4.4	-6.0-2	-	[21]

Despite the many mentioned advantages, there are still several challenges regarding the manufacturing and in-service capabilities of these attractive materials. Namely, the relatively high cost of material, high exposure of polymeric waste [26], the sensitivity of the composites to high temperature and flammability [27,28], low thermal conductivity and consequently fouling and icing of the structure [29,30], bio-incompatibility or toxicity of specific constituents for human organs [31,32], and limited anisotropic electrical conductivity, which is also favorable at times [33–35]. Moreover, the nature of the polymeric matrix directly affects the manufacturing, properties, and processability of the FRPCs. The application of thermoplastic-based composites is highly limited due to the abundant manufacturing defects caused by the high viscosity of the polymer hindering appropriate coverage of fibers and consequently defective structure [36]. In the case of thermosetting composites, however, owing to the low viscosity and proper flow of the resin, the fibers can be fully wet-out, highly reducing the defects [37]. This has led to the development of several manufacturing methods, such as hand lay-up, pultrusion, filament winding, liquid composite molding, and automated fiber placement to fabricate composite parts satisfying various designs.

1.2. Coating and Surface Metallization of FRPCs

Many of the issues regarding the performance of FRPCs arise from the phenomena on the surface of the material and can be resolved by surface modifications [38]. To illustrate, icing and strike of lightning on airplane wings made of FRPCs due to low thermal and electrical conductivity [39,40], both high-velocity impact causing damage on radome of planes and low-velocity impact fatigue [41], flammability of structures such as ship hulls [42], and erosion damage of wind turbine blades [43] are cases that can be adjusted through surface engineering. However, due to the characteristics of FRPCs, their coating or metallization process possess several ambiguities. To

briefly elucidate, based on the nature of the polymer matrix (thermosetting or thermoplastic) surrounding the reinforcing fibers, the composite might get eroded or deformed through partial melting and experience melting/solidification cycles, respectively, upon contact with impinging particles from thermal spray [44]. On the other hand, direct surface metallization of thermoplastic matrix FRPCs is proven to be more feasible compared to thermosetting ones [45].

Regardless of the polymeric matrix type, surface metallization of FRPCs has been successfully achieved through several thermal spraying methods such as dynamic cold spraying (CS), flame spraying, twin wire-arc spraying (TWAS), air-plasma spraying (APS) [46], and even high-velocity oxygen fuel (HVOF) [47]. Apart from the material being deposited, the main distinguishing idea of each study is the employed method to engage the coating with the PMC to enhance the adhesion strength without deteriorating the substrate. Namely, electroplating, or thermal spraying of thin metallic bond coat [48], applying a blend of garnet grit/epoxy [49], spraying a mixture of metal/thermoplastic powder [50], and more recently incorporation of a metal wire mesh on the uppermost surface of the PMC (Figure 1.1) have been explored [51]. Accordingly, the latter approach can provide a versatile anchor for the coating with robust adhesive strength, though conditional on the exposure level of the metal mesh. Considering that the exposure is achieved through mechanical surface preparation (i.e., grit-blasting), either development of other methods or optimization of the grit-blasting process is a must to provide a uniform texture of roughened metal mesh (proper-blasted) rather than resin-rich area (under-blasted) or exposed PMC (over-blasted) substrate.

Up to date, the grit-blasting process and inspections during surface preparation for exposing metal mesh have been done manually based on the operator's expertise. Thus, developing an accurate

method enabling fast-paced examination on a large scale is essential to present the real industrial application of surface metalized FRPCs via thermal spray.

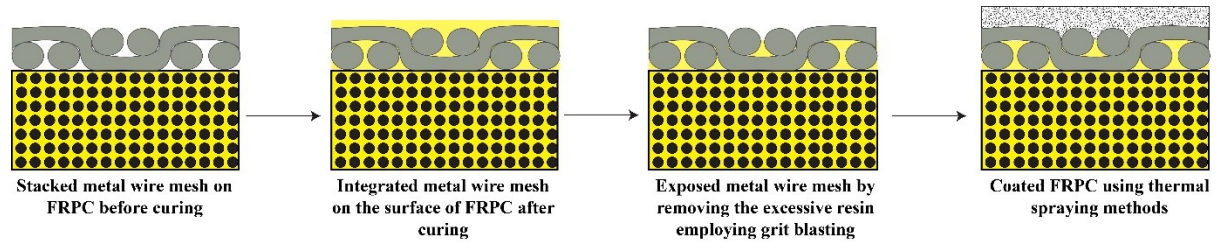


Figure 1.1. A schematic representation of preparing FRPC for thermal spray coating by incorporation of superficial metal mesh in the system and grit-blasting.

1.3. Surface Preparation Prior to Coating

The coating is a surface phenomenon; thus, preparation prior to surface coating is the keystone of successful processing. Surface pretreatment is carried out to render adherend surfaces receptive to the formation of strong, durable, and adhesive coatings. It is therefore required to expose the basic adherend material directly to the coating material without intervening layers of oxides, paints, and other contaminations. The presence of undesirable, weak boundary layers leads to a lack of direct contact of adherend material to the substrate surface, and consequently deviation from the formation of a coating with high adhesion strength [52]. Factors such as the nature of the substrate, the component size, and the coating method determine the selection of the surface preparation method. Table 1.2 summarize the various developed surface treatment processes along with their effect.

In the case of the metallic substrate, vapor degreasing with an organic solvent or other effective aqueous systems followed by grit blasting to increase the contact surface area by roughening the surface is required. Further, chemical etching can remove weak oxides and form oxides that are well bonded to the bulk of the part. Also, priming is an effective method to protect the metallic

surface from oxidation prior to the coating process. In contrast, low-energy surfaces and mainly plastics require completely different types of surface preparation altering the chemical nature of the surfaces. Nevertheless, the application of fine abrasive paper (sand, carborundum, or aluminum oxide-abrasive grit/metal, or oxide) is pronounced for abrasion of thermoset surfaces [53].

Table 1.2. Common surface preparation methods and their effect on metals and polymers [52].

Treatment method	Effect of treatment
Degreasing	Cleaning of the surface
Grit blast	Loose material (weak boundary) removal from the surface and increase in contact surface area
Acid etching	Surface oxidation
Corona treatment	Weak boundary layer removal and surface oxidation
Flame treatment	Weak boundary layer removal and surface oxidation
Chemical etching	Weak boundary layer removal and surface oxidation, Surface defluorination and oxidation

1.4. Aims and Objectives

Despite numerous attempts to develop a technique for surface metallization of FRPCs, there are still debates on the advancement of a method enabling the formation of coating with desirable properties and being practical on large scale, while yielding low environmental damage. In this regard, the recent designs for the incorporation of metal wire mesh into the outermost layer of FRPC have great potential. However, the surface preparation of the system using grit-blasting is not studied comprehensively up to now. The existence of several processing parameters and lack of automation, and consequently accuracy, is a prime motive to further develop this technique for industrial applications. In this study, it is aimed to:

- Fabricate metal mesh incorporated CFRPs laminates employing prepregs and hand lay-up technique, followed by curing in an autoclave to explore repeatability and possible issues during composite manufacturing.
- Design and assembly of an automated setup for grit-blasting of fabricated metal mesh/CFRP system eliminating operator experience from the surface preparation parameters.
- Investigate the effect of main grit-blasting parameters on the metal mesh/CFRP and identify a quantitative measure to optimize the process.
- Generate operational parameter maps as a reference for future works enabling estimation of surface preparation state.
- Explore capabilities of in-expensive, portable digital microscope for in-situ inspection of the system in a non-destructive manner.
- Mine data sets for developing an image processing method that can entirely automate the process by real-time inspection of the part throughout the process providing feedback on the state of surface preparation, calibrating the parameters, and determining the requirement for further surface pre-treatment.

1.5. Thesis Outline

This thesis is organized into 5 chapters as follows.

Chapter 2 delves into the recent advancement of FRPCs elucidating why surface coating of this class of material is in-demand. Also, Coating methods for FRPCs are outlined proving the merit of thermal spray ones, as well as an introductory on the grit-blasting process. Afterward, chapter 3 focuses on the methodology and experimentation conducted in this study. Chapter 4 is put

forward to present the results and discuss the data extracted. Ultimately, Chapter 5 summarizes the conclusion of this study along with a suggestion for future research.

Chapter 2: Literature Review

2.1. Fiber Reinforced Polymer Composites (FRPCs)

In this section, the main constituents of FRPCs are highlighted demonstrating their properties and application. More importantly, the drawbacks are summarized providing reasons for the importance of surface coating for this class of material to enhance their functionality and sustainability.

2.1.1. Fibers

The exquisite constituent of PMCs is the reinforcement phase, which exists in the forms of particles, fibers, and whiskers. The reinforcements dispersed in the matrix are primarily responsible for enhancing the properties of the matrix, especially bearing the applied load to the composite [1]. Among the different forms of reinforcements, not only the handling and formability of fibers are advantageous, but also, they result in better load transfer from the matrix to the reinforcement because of the high aspect ratio providing more surface [54]. Fibers are classified based on their materials and architecture. From the materials point of view, fibers are either natural or synthetic (such as glass, carbon, graphite, aramid, boron, SiC, polyester, etc.). Commercially available synthetic fibers are in structural forms of chopped, monofilament, tows, or fabrics with various structures like woven, non-woven, knitted, and braided, each of which affects the properties of the fabric [2,3].

Silica-based fibers, known as glass fibers (GF), present high specific stiffness and strength, high corrosion resistance, electrical insulation, excellent fatigue behavior, and low cost, and are extensively applicable in aerospace, automotive, energy sectors, and electronics, and structural. Nonetheless, the major drawback of brittleness leads to the troublesome handling of this class of fibers. As a result, employing sizing for more facile handling is crucial, which must be further eliminated and replaced by coupling agents and functional coatings to obtain suitable interphase

with the polymeric matrix during composite manufacturing. Apart from that, different classes of glass fibers yielding specific properties have been developed up to now. For instance, A-glass fibers provide higher durability, strength, and electrical resistivity, while C-glass or D-glass fibers offer corrosion resistance and low dielectric constant, respectively [55]. Growing concern over GFRPCs is the environmental pollution caused by the waste scraps disposed of on landfill grounds [56]. Moreover, uptake of moisture by glass fibers is another challenging issue since it leads to degradation of mechanical properties of the composite and subsequent failure [57]. GFRPs are also applicable in fields of electrostatic dissipation, electromagnetic shielding, and absorption through functionalization. Although electrically conductive GFRPs have been already developed using conductive particles or mesh, they suffered from interfacial corrosion, thermal expansion coefficient mismatch, and weaker mechanical performance.

Carbon fibers (CF), consist of more than 90 wt.% carbon in the form of graphene layers with a mixed turbostratic arrangement in the core of the fiber and parallelly aligned along the fiber axis at the skin (which depends on its precursor and post-heat treatment). Indeed, the precursor directly influences the microstructure leading to the capability of producing CFs with diverse properties. As a result of the particular arrangement and the strong C-C covalent bonds oriented parallel to the fiber axis, CF displays high strength and modulus, great thermal stability and chemical resistance, low coefficient of thermal expansion, high conductivity, and especially low density, all which give rise to the application of this class of fibers in aerospace, automotive, marine, civil construction, energy sector, leisure equipment, and biomedical [58,59]. Despite the many advantages of CFs, they pose few but severe limitations, namely brittleness and lack of oxidation resistance of fibers in composite, requiring surface activation, health risks, waste management issues, and high price [60,61].

2.1.2. Polymer Matrices

In general, the matrix phase of a PMC plays crucial roles such as (i) surrounding the reinforcements and providing the ability of PMC to be shaped while keeping the reinforcements in place and in right alignment, (ii) transferring the applied loads to and between the reinforcements through shear stresses at the interphase, (iii) bearing the applied compressive and shear loads (especially in the case of FRPCs, since fibers are incapable of bearing high magnitude of these forces), (iv) protecting the reinforcements from environmental conditions, namely corrosive media and moisture, and also (v) enabling other functions like resistance to flammability [62]. Fundamentally, a polymer constitutes rather small molecular chains (monomers), which are joined together by covalent bonds to form long chains through the polymerization process. The selected monomers (resins), initiator, other additives, and polymerization process are the influencing factors on the characteristics (to name a few, molecular mass, glass transition temperature, and viscosity) of the obtained polymer and the non-/existence of by-products [63,64]. Therefore, it is crucial to broaden our knowledge about various polymers and polymerization processes for a more effective material selection and design of polymer composite manufacturing methods harmonic with the desirable properties and nature as well. A brief introduction of thermosetting and thermoplastic polymers, two of which are quite attractive in the field of FRPCs, is presented in the following of this section shedding light on the characteristics, applications, and drawbacks of currently developed systems.

2.1.2.1. Thermosetting

The main distinguishing characteristic of thermosetting polymers is their response to elevated temperature. A hardened thermoset polymer is the result of a cured soft solid or viscous liquid resin, chains of which are cross-linked building a network structure using curing agent molecules. The cross-linking reaction, which is usually taken place at high temperatures and under pressure,

is irreversible (for conventional resins). Therefore, the hardened thermoset will burn to char upon heating instead of melting, which makes their recycling a challenging issue. The network structure gives rise to higher mechanical properties by restraining the chains from sliding on each other. That also means, that increasing the density of cross-links leads to higher hardness and stiffness (lower toughness), better resistance to chemical attacks, greater durability, and less prone to thermal degradation [3,65,66]. The parameters affecting the selection and feasibility of a thermoset polymer as a matrix for FRPC include, but are not limited to, (i) physical properties of the resin (especially its viscosity), (ii) its capability in wetting the reinforcements, and the corresponding interactions, (iii) thermal stability, (iv) low shrinkage after cure, (v) the achievable mechanical properties and functionalities, (vi) production rate, and (vii) cost [66]. Among the many existing thermosets, there are only a few compounds that satisfy the aforementioned criteria, to name a few, epoxies, polyesters, vinyl esters, polyurethanes, and bismaleimides.

2.1.2.1.1. Epoxies

The epoxies, identified by the glycidyl or epoxide group (-CH-O-CH-) in their molecular structure, are considered the most important polymer matrices. This is a result of their superior mechanical strength, low density, good wetting properties, good chemical and electrical resistance, fire retardancy, and low shrinkage, all of which make this group applicable in aerospace, automotive, construction, and electronic industries [67,68]. There are numerous epoxy systems commercially available, however, the most common one is diglycidyl ether of bisphenol-A (DGEBA), which possesses two epoxide groups in its chains [54]. Other complex epoxy systems, such as 9,9,10,10-tetrakis (4-hydroxyphenyl) anthracene (TGETA) and Novolac, contain more aromatic rings and epoxide groups yield higher mechanical properties and thermal stability. Aside from the epoxy resin, the employed curing agent and other additives play crucial roles in the processability and

final characteristics of an epoxy matrix [69]. Recently, investigations on the behavior of various bisphenol-A based epoxy matrix composites cured using different hardeners, demonstrate that increasing the exothermic heat generated during curing leads to a perfect polymerization of the system, and subsequently greater thermo-mechanical properties [70].

A challenging issue regarding the properties of epoxies is their brittleness. As already mentioned, increasing the cross-links density results in greater mechanical strength, but also brittleness of the structure. Although it is possible to toughen the structure by reducing the cross-links, it is not a favorable solution since it reduces the glass transition temperature (T_g) of the polymer as well. In this regard, studies proved that it is practical to enhance the toughness of epoxy by modifying its structure using other substances such as tertiary-amine-terminated rubbers [71]. This way, it is not only possible to enhance the toughness, but also T_g can be increased.

2.1.2.1.2. Polyesters

Polyesters, and primarily unsaturated polyesters (UPE), frame another useful group of polymer matrices, molecular chains of which are constituted from various diacids and diols (most prominently, propylene glycol and maleic anhydride), yielding ester linkage (C-O-C=O) in the structure. UPEs are less expensive than epoxies and display low viscosity, which can be an advantage for the manufacturing sector, however, they have weaker mechanical performance, and tailoring their properties can be more challenging [37,54]. One of the UPEs characteristics is the existence of double-bonded carbons in their structure, which is considered a reactive site, making low-viscosity liquid UPEs likely to be cross-linked even at room temperature. Therefore, inhibitors are added to their blend to achieve enough shelf life, while they are being cured by the addition of initiators, curing agents, and catalysts [72]. Although UPEs are not as flexible as epoxies for being characteristically tailored, they yield a set of properties based on their constituents and degree of

cure that make them applicable in marine, construction, automotive, and household equipment [73]. The major challenges for employing UPEs are namely, reduction of styrene exposure content, improving mechanical properties (especially toughness), enhancing fire and heat resistance, and minimizing its volume shrinkage as a result of curing [74].

2.1.2.1.3. Vinyl Esters

Vinyl esters comprise a very useful type of thermosetting resin system, which present an intermediate set of properties between those of polyesters and epoxies. Indeed, they are produced by the reaction of epoxies and unsaturated carboxylic acids. Vinyl ester resins (VERs) contain C=C bonds in their molecular structure similar to UPEs, however, the density of these crosslinking sites is less and inclined toward the end of chains in the case of VERs [75]. Better mechanical properties, especially toughness, and thermal stability in comparison to polyesters, besides the lower cost and more facile curing compared to epoxies, make VERs an appealing choice of the matrix for FRPCs applicable in a broad range of industries such as transportation, marine, gas vessels, civil infrastructures, and energy sector [76]. Despite the many advantages, VERs are susceptible too. Flammability, the release of environmentally toxic substances, and degradation of mechanical properties due to temperature rise and moisture are among the most challenging issues.

2.1.2.1.4. Polyurethane Resins

Polyurethanes (PUs), formed from the addition polymerization of polyols and polyisocyanates, comprise a group of low-viscosity thermosetting polymers posing fascinating strength, toughness, and low volume shrinkage, offering excellent surface finish, and befitting automotive industries, leisure equipment and most recently in medical applications [37,72]. As a result of the molecular structure of PUs, which consists of a soft and a hard segment (i.e., polyol and isocyanate, respectively), the properties can be tailored by employing various raw materials.

2.1.2.1.5. Bismaleimide Resins

Bismaleimide (BMI) resins are among polymer matrices suitable for structural fiber reinforced composites with high-temperature performance coupled with great mechanical properties, low viscosity, and low volume shrinkage [72,77]. Although BMI resins are developed to both offer high performance and reduce the cost (inexpensive in comparison to analogous alternatives) they possess a major drawback, i.e., brittleness of the cured system [78].

2.1.2.2. Thermoplastic

Contrary to thermosetting polymers, thermoplastics can undergo multiple cycles of heating and cooling without experiencing significant damage. This behavior arises from the simple molecular structure containing physically entangled macromolecules (and not chemically bonded) [79]. Although such behavior allows for easier recycling, weldability, and reduction of cost both in terms of storage and fabrication, the consumption of thermoplastics as a matrix for fiber reinforced composites is highly limited compared with thermoset resins. The primary restricting parameter is the high viscosity of thermoplastics obstructing the impregnation of fibers comprehensively, which leads to the fabrication of imperfect parts [80]. In spite of that, advanced long fiber reinforced thermoplastic matrix composites (FRTPs) have been developed to exploit the above-mentioned advantages along with higher ductility, environmental resistance, and lack of release of volatiles during fabrication. Accordingly, thermoplastic polymers such as polypropylene (PP), polyetheretherketone (PEEK), polyetherketoneketone (PEKK), polyethersulfone (PES), polyetherimide (PEI), and polyphenylenesulfide (PPS) are among the most selected matrices for this class of FRPCs [54]. To manufacture advanced thermoplastic matrix FRPCs, it is essential to achieve a high fiber volume fraction along with high interfacial shear strength between fibers and matrix. In this regard, studies reported that using the solution impregnation molding method, it is

possible to lower the viscosity of the thermoplastic matrix and achieve volume fractions as high as 60%, which leads to mechanical properties comparable with thermosetting CFRP [81]. In order to enhance IFSS, surface treatment of the fibers is crucial. Investigations on adhesion of CNT fibers/PEKK prepared by an electro heating curing, which leads to melting of the thermoplastic matrix and better impregnation of fiber bundles, suggest the feasibility of this method for enhancing IFSS of advanced thermoplastic FRPCs [82].

2.2. Coating methods for FRPCs

A major aspect of FRPCs that has been proportionally less explored by scientific and industrial societies is surface engineering and coating of this class of materials. Indeed, engineering the properties of FRPCs through surface coating can be considered a promising solution for both extending the application range of these composites and reducing their waste and maintenance costs, which can lead to sustainable development. In this section, the most renowned coating methods are briefly introduced highlighting their capabilities and limitations in the case of depositing protective and functional films on FRPC substrates.

2.2.1. Thermal Sprays

Thermal spraying methods utilize heat sources and carrier gases to melt/semi-melt the feedstock material in the form of powder/wire, and to propel the atomized particles toward the substrate to be deposited shaping lamellar (splat) structure [83]. Different methods of thermal spraying are not only developed to deposit a wide range of materials but also to achieve depositing particles with various factors (particle temperature, velocity, size) resulting in coatings that meet the desired criteria (porosity, adhesion, functionality, etc.).

2.2.1.1. Flame Spray

Flame spraying, the oldest thermal spray method, utilizes the high temperature of gas combustion flame (approximately 3000 °C, depending on the gas-oxygen ratio) as the heat source for melting the powder/wire feedstock [84]. Although the method is highly cost-efficient, factors such as relatively low adhesion of the coating, high porosity, and oxide content [85], along with the involvement of flame in the process make its application for FRPCs (which can be flammable) limited. Indeed, due to the low in-flight particle velocity, the standoff distance of the gun with the substrate has to be minimized (in the range of 150-250 mm [86]) in order to reduce the content of oxide in the coating [87], which can increase the risk of deteriorating the polymeric base substrate. However, Studies demonstrated applying a garnet sand/epoxy on the FRPC substrate (Figure 2.1) prior to flame spraying limits the heat transfer and hinders the degradation of the composite during flame spraying of Al-Si and NiCrAlY on FRPCs [88,89].

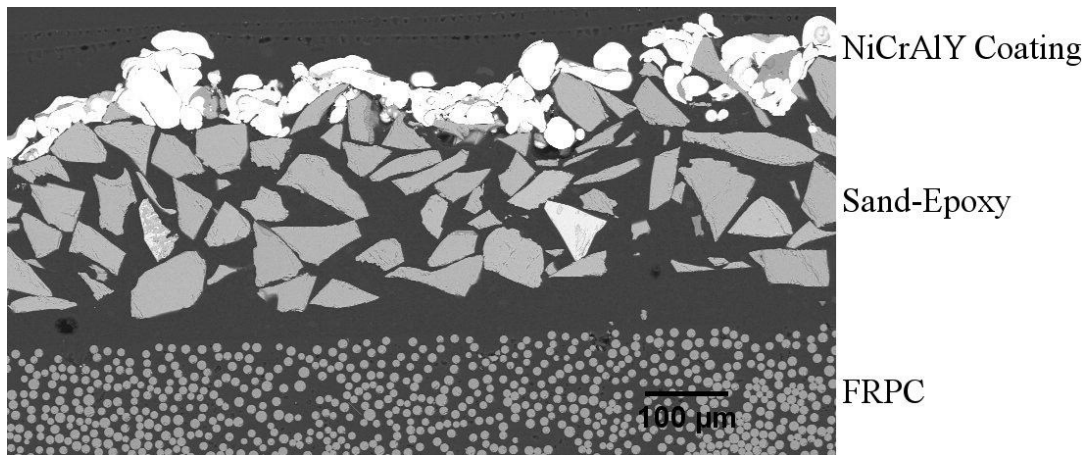


Figure 2.1. Scanning electron microscope image of a developed surface coating on garnet sand roughened FRPC sample [89].

2.2.1.2. Wire Arc Spray

Twin wire arc spray gun utilizes electrical direct current to generate an electric arc between two conductive consumable wires reaching a temperature of 4000-6000 °C. The high temperature of the arc melts the wire feedstock, and the flow of compressed air or noble gases (to reduce the oxidation) atomizes the molten wire feedstock accelerating particles with a velocity of 50-150 m/s toward the substrate. The high spraying rate combined with the low power consumption makes this method remarkably economical. Moreover, the capability to spray various materials in the feedstock form of cored wire widens its application [90]. Controlling the current, atmosphere, feeding rate, substrate temperature, standoff-distance, and surface treatment of substrate are the crucial parameters that allow for coating of low melting point substrates employing wire arc spraying [91–93]. In this regard, laser texturing on the surface of the substrate has been proven as an effective method for surface preparation leading to higher adhesion of the coating to the substrate as a result of mechanical anchoring of particles [94]. Moreover, it is suggested that deposition of pure zinc bond coat, which has a suitable wettability on non-metallic substrates can be a promising solution to form a build-up coating on PMCs [95]. Also, studies on coating thermoplastics employing wire arc spraying indicate that it is challenging to deposit metals with low density and/or high melting point on thermoplastics with high impact strength since the particles either do not have enough momentum to adhere to the surface or they cause localized melting and lack deposition [96].

2.2.1.3. Plasma Spray

Plasma spraying is a powerful tool utilizing a DC-generated electric arc between the copper anode and tungsten cathode to ionize the primary plasma gas (i.e., Ar or He), which forms a plasma jet upon reaching a sufficient level of energy for recombination of free electrons and gas ions. The

formation of a plasma jet releases a significant amount of energy and light increasing the temperature as high as 15000 °C, which acts both as the heat source for melting the feedstock and drag force for accelerating the molten particles toward the substrate. Even though plasma spray is extensively used in industry, it suffers from the torch arc instabilities and wears of tungsten electrode [97,98]. It has been reported that, in addition to secondary plasma gases (i.e., H₂ and N₂), modulated current can be used instead of power input to better control the arc fluctuations, which affects the properties of plasma jet and subsequently the coating [99]. In terms of feedstock, developed dry powders, wires [100], suspensions (SPS), and solution precursors (SPPS) are available [85]. In fact, the limitation associated with spraying nano and ultrafine dry powders obliged the development of SPS and SPPS. The major benefit of plasma spray, aside from the low content of oxide, is the ability to deposit from highly dense to porous coatings with acceptable adhesion by varying the spraying parameters [101]. Aside from the application of plasma spray in the deposition of coatings, especially thermal barrier coatings (TBCs), on metallic substrates [102], recent studies indicate the practicality of metallization of polymers and low melting point substrates employing plasma spray methods [103–105]. Indeed, implementing a powder filler layer, Cu powder [106], Al bond coat [107], and metal wire mesh [51] prior to plasma spraying are reported to be practical measures for successful deposition of the coating on FRPCs (Figure 2.2).

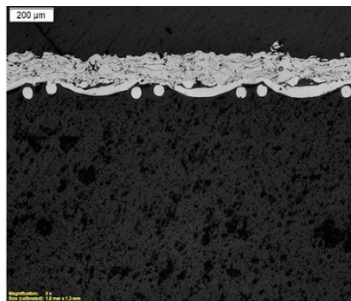


Figure 2.2. Cross-section of a coated metal mesh/ FRPC substrate using plasma spray [51].

2.2.1.4. High-Velocity Air/Oxygen Fuel (HVAF/HVOF)

Continuous ignition in a combustion chamber filled with a mixture of fuel in liquid or gas phase with oxygen or natural air generates a high-velocity stream of hot gas, shaping a thermal spray being released into a nozzle. Providing a high temperature of up to 3000 °C and accelerating the feedstock particles to a speed of 600-1200 m/s (based on the type of fuel and oxidant gas composition), HVOF and HVAF realize deposition of highly dense coatings with superior adhesion compared to plasma-sprayed ones. The kinematic energy of sprayed semi-molten particles using HVOF and HVAF is high enough to damage the surface of polymeric and FRPCs, but the two methods may be a potential tool for applying coatings on surface modified (e.g., using bond coat and/or metallic mesh), low melting point and soft substrate. Recent investigations report the successful deposition of Al-Si coating on FRPCs employing intermittent HVOF spraying and cooling substrate with compressed air [108].

2.2.1.5. Cold Spray

Cold spray utilizes heated, highly compressed gas introduced to a converging-diverging nozzle, which allows for reaching supersonic velocities. The high-speed gas accelerates the impinging solid particles bringing them to a critical kinematic energy level so that they either deform plastically upon impact on the substrate surface or penetrate it. Therefore, optimizing the spraying parameters, that is gas pressure and temperature, particle size, and spraying distance is vital to achieving a coating. Although the sprayed particles are in solid form and relatively cold, the kinematic energy of the particles is intense to erode polymeric and FRPC substrates similar to HVOF/HVAF. But on the contrary, successful deposition of low melting point powders on thermoplastic substrates has been reported [109], proving the potential use of the cold spray for metallization of FRPCs. Several studies focused on the deposition of Sn coating on FRPCs

utilizing cold spray revealing the higher deposition efficiency at lower temperature and pressure (below 500 K and 60 psi) and revealing erosion of composite and fracture of fibers upon increasing the value of CS parameters [110–112].

2.2.2. Electroless Deposition

As a sub-category of electroplating methods, electroless deposition enables the formation of metallic coatings on various substrates, especially electrically non-conductive and low-conductive ones. Principally, the redox electrochemical reactions are utilized to form metallic cations, which will be delivered to the surface-activated substrate via an electrolytic solution. In this regard, controlling the temperature, composition, and pH of the solution using additives, catalysts, and stabilizers is crucial to achieving full coverage of substrate by the depositing species [113]. The method requires rather simple equipment, provides uniform coating thickness, and it is especially suitable for depositing palladium, nickel, silver, and Cu [114], however the complex chemistry of the solution bath as well as the involvement of environmentally pollutant solutions are considered as unresolved issues associated with this method [115]. Considering the discussed environmental impact and the reported advantages of broadening the application of polymers and FRPCs [116–119], electroless deposition can be a promising method for the development of coatings for advanced FRPCs, if the hazardous solutions are abated, refined, or disposed of properly.

2.2.3. Chemical Vapor Deposition (CVD)

In the CVD process, the chemical reaction of volatile compounds of the depositing material with other gases in a reactor, where the substrate is placed and heated, results in the formation of solid atomic scale deposition. Using various stoichiometry and controlling the temperature of the substrate, CVD is capable to deposit different materials with single-crystalline, polycrystalline, nanocrystalline, epitaxial, and amorphous structures [120,121]. Several strategies have been

implemented to facilitate the triggering of desired chemical reactions, nucleation on the substrate, and film growth. In this regard, plasma-enhanced CVD (PECVD), metal-organic CVD (MOCVD), laser-assisted CVD (LACVD), and aerosol-assisted CVD (AACVD) are some of the developed systems. Two issues regarding CVD processing are the requirement for a substrate with high heat resistance and the release of hazardous gas by-products [122]. Nevertheless, several studies prove the successful application of PECVD and MOCVD in surface metallization (Cu deposition) of FRPCs [123–126]. However, one major drawback of this method is the low deposition rate, which can adversely affect its industrial application.

2.2.4. Physical Vapor Deposition (PVD)

PVD is a versatile method using various heat supplies such as electron beam, laser, ion beam, resistant-heated wires, and cathodic arc to heat the target material (feedstock) to vaporization/melting point, where the target atoms will evaporate, passing through vacuum and condensate on the substrate surface. The PVD process utilizing optimized parameters (the vacuum, materials selection, and substrate) enables atomic deposition of thin films with high adhesion and low porosity [127]. Although employing PVD it is possible to deposit almost any compound in a clean and environmentally friendly manner, high cost along with low deposition rate and difficulty in forming uniform coatings for complex shapes limits its application [128]. Despite the disadvantages, successful deposition of Ti/TiN on CFRPs to enhance erosion resistance [129–132] and chromium on polymers [133] demonstrate the potential of PVD in future surface coatings of polymer composites.

2.3. Grit-blasting

Grit-blasting is a crucial process involving the spray of abrasive particles using compressed air on the surface of a part, to be coated afterward by thermal spraying, mainly to obtain a rough surface

that can mechanically anchor the impinging particles and subsequently form a surface coating with high adhesion strength [134]. Despite that, the process can clean the surface from superficial oxides and contaminants as well. the grit-blasted part must be cleaned once more (often using compressed dry air) to remove the residues of grit-blasting [135]. The process parameters, that is compressed air pressure, standoff-distance, exposure time, grits material, feed rate, grits size and distribution, spraying angle, and effective radius of blasting, affect the surface properties of the substrate [136]. There are two types of grit-blasting machines that are slightly different, namely suction blasting and pressure blasting.

Suction blasting uses the Venturi principle which is the reduction in pressure that results when a pressurized air flows through a constriction. The reduced pressure draws grits from a non-pressurized hopper through a valve where induction air mixes with them. The induction air/grits stream flows to the blast gun combines with the compressed air stream and propels toward the target (Figure 2.3 a). Pressure blasting makes use of a pressurized vessel retaining the abrasive media. However, while the blaster is not blasting, the tank is not under pressure. The vessel has a pop-up valve withinside the pinnacle that lets in media to go into the pot while it is not pressurized. When the blast gun is activated, the tank is pressurized because the pop-up valve closes and seals the tank. The air pressure withinside the vessel and the blast hose line will become the same. This means that there may be no difference between blasting pressure and vessel pressure allowing the abrasive media to control the valve and into the compressed air stream at the blast pot and out to the nozzle (Figure 2.3 b) [137].

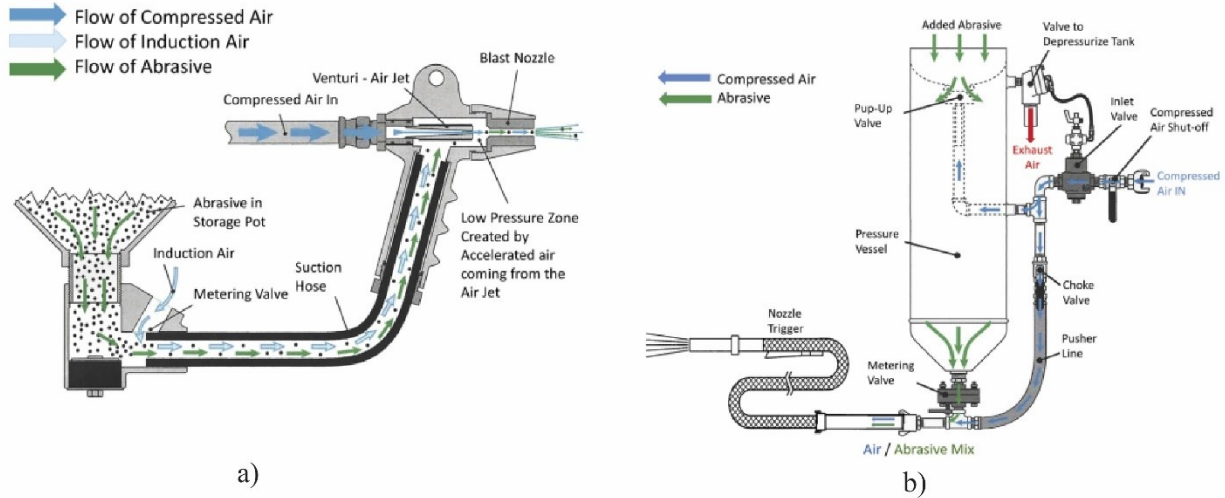


Figure 2.3. Schematics of a) suction blasting and b) pressure blasting equipment [137].

There exist several grit materials, the choice of which depends on the intended purpose, the substrate, and the cost. Properties of common abrasive media are summarized in Table 2.1 along with their relative costs. The grit must be harder than the substrate used to roughen it. Also, it is worthwhile of mentioning that denser materials have more momentum and impose more energy on the substrate.

Table 2.1. Properties of commercially available abrasive media for the grit-blasting process [137].

Media	Hardness (Moh)	Density (g/cm ³)	Bulk Density (g/cm ³)	Relative Cost, Volume Basis
Walnut shells	1-4	0.64-1.28	19	-
Silicon carbide	9	3.2	1.52	50
Aluminum oxide	9	3.8	2.00	25
Glass bead	6	2.2	1.60	18
Plastic grit	3-4	1.45-1.52	0.72-0.80	30
Steel shot	6	7.87	4.49	27
Steel grit	6	7.87	3.68	-
Sand, silica	7	2.6	11	-

Chapter 3: Experimental and Analytical Methodology

3.1. Fabrication of Metal Mesh Incorporated FRPC

In order to fabricate the metal mesh/FRPC system, CYCOM® 977-2 prepregs (carbon fibers pre-impregnated with epoxy resin and partially cured) and stainless steel 316 wire mesh of 200 are utilized. The prepreg roll was taken out of the freezer and kept at the room condition for one hour allowing the temperature of the prepreg to rise to room temperature. This way, the viscosity is reduced

so that it is possible to cut the prepreg into desirable sheets. The prepregs were cut into 29.5-31.5 cm² laminas. A tool is prepared for delivering the shape and surface finish of the composite through cleaning with acetone and applying a release agent for facilitating the removal of the composite after curing. A unidirectional laminate containing 20 layers of CFRP prepreg (i.e., [0]₂₀) is laid up on the prepared tool. Thereafter, metal mesh cleaned with acetone is stacked on top of the laminate, followed by an aluminum caul plate keeping the metal mesh in position. A microscopy image of the metal mesh is observable in Figure 3.1. Also, the nominal properties of the metal mesh are summarized in Table 3.1.

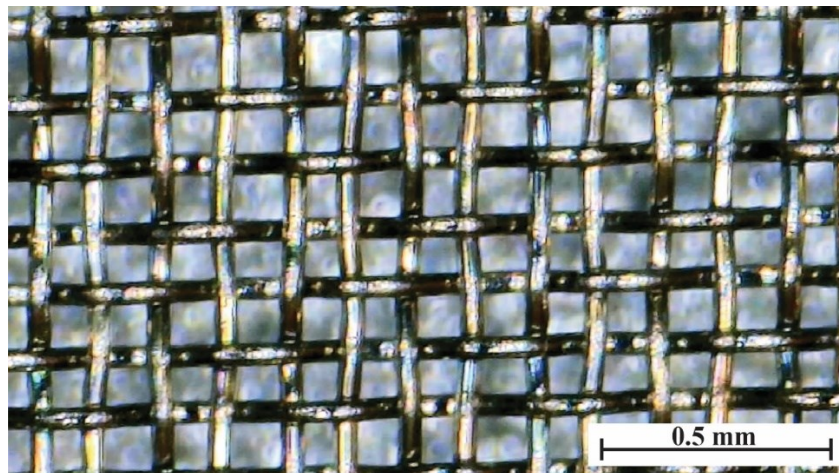


Figure 3.1. Digital microscope image of 316 stainless steel metal mesh 200.

Table 3.1. dimensional characteristics of 316 stainless steel metal mesh 200.

Mesh count	Nominal aperture (µm)	Thickness (µm)	Wire diameter (µm)	Open area (%)	Weight (kg/m²)
200	74	124-120	53	34	0.28

Then, the laid-up system is vacuum-bagged using four items, including vacuum bagging film, release film, breather, and bleeder cloths. The peel ply positioned on the caul plate is another part of the vacuum bagging setup that eases the removal of the part from the bagging materials as the part is cured. Breather and bleeder cloths are applied sequentially on the peel ply serving as channels for airflow throughout the laminate. To illustrate, the vacuum connector is installed directly on top of the breather, to pull out the air and gases emitted during the curing. Further, the bleeder cloth absorbs the extra resin from the part. The vacuum bagging film, sealed around the tool employing sealant, as the outermost layer of the bagging set up creates the airtight seal and stretched over the composite and other items, which also renders a close mold. Finally, the bagged system is connected to a vacuum pump by a hose and vacuum connector to complete the vacuum bagging. An important parameter regarding vacuum bagging is the distance of the vacuum hose from the composite, as it can adversely affect the uniform flow of the resin through the metal mesh. A schematic of the vacuum bagging setup is presented in Figure 3.2.

It should be considered that the vacuum bagging both helps with the elimination of the trapped air between the layers avoiding delamination, and with the removal of the excess resin from the composite, which in this case can flow through the porosities of metal mesh, covering it and integrating it into the composite structure. Vacuum bagging will further improve samples' physical properties leading to the manufacturing of a composite part with a higher fiber volume fraction compared to typical hand lay-up counterparts.

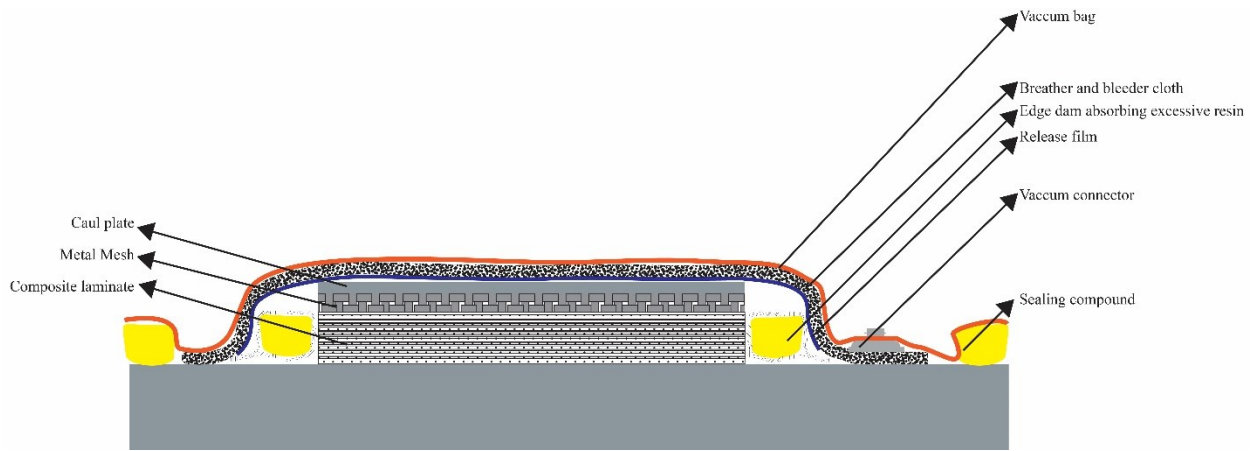


Figure 3.2. A schematic representation of vacuum bagging setup of metal mesh/FRPC.

Afterward, the vacuum bagged setup is placed in an autoclave for the curing process. An autoclave is used for the simultaneous application of high temperature and pressure. Figure 3.3 depicts the heating cycle and applied pressure on the setup for curing the metal mesh/CFRP composite. It is worthwhile to mention that the applied pressure is slightly lower than the suggested value by the prepreg manufacturer, however, the curing time is increased to achieve fully cured and strong composite panels. Indeed, the temperature is raised at a rate of 2.5 °C/min reaching the curing temperature of 180 °C. The temperature is then kept almost constant for 6 hours leading to a reduction of epoxy resin viscosity and its flow and further initiation of cross-linking and curing. The autoclave is then cooled down with a low rate of 0.25 °C/min. in the case of pressure, the valve is modulated to 5 bar, so that it increases gradually at the beginning, and it is set to lift the pressure after 10 hours. The high pressure contributes to the compaction of the FRPC and obtaining a high fiber volume fraction.

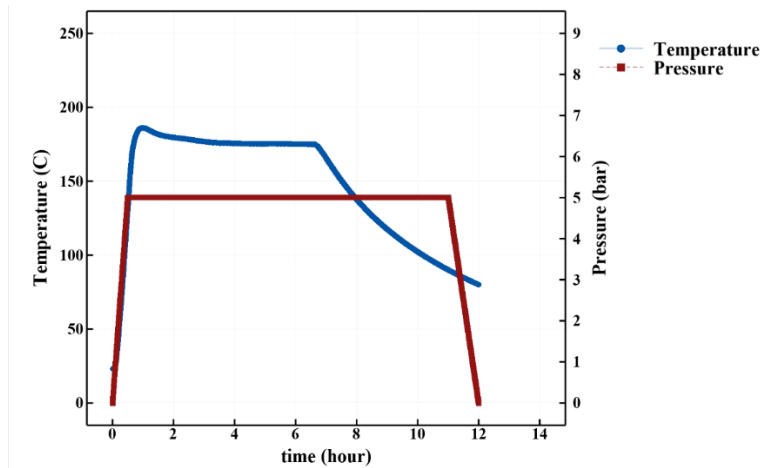


Figure 3.3. The applied heat cycle and pressure on the system during the curing stage in the autoclave.

The vacuum bagged setup is carried out of the autoclave, and the bagging is removed to de-mold the panel from the tool. Figure 3.4 displays the fabricated metal mesh/CFRPs with two different vacuum bagging setups (i.e., the gap between vacuum gauge and laid-up composite). It can be deduced the very small gap between the gauge and part can lead to the suction of the excessive resin, which is absorbed by the installed dam around the part. This causes a lack of flow of resin up, through the metal mesh and achieving a failed part.

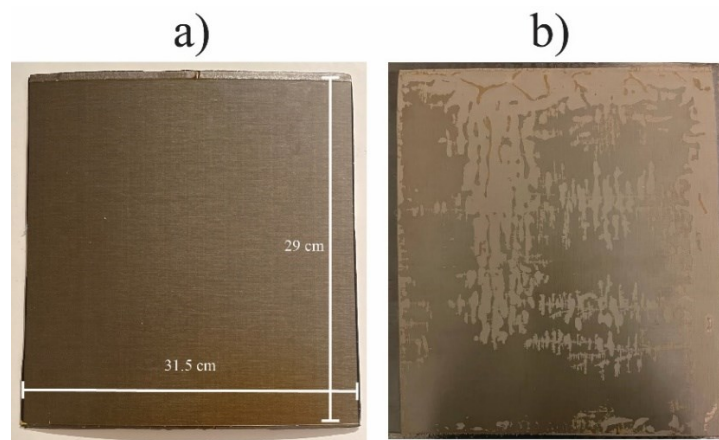


Figure 3.4. Images of As-fabricated metal mesh/CFRP plates, a) showing a perfectly manufactured plate, while b) demonstrate lack of complete coverage of metal mesh by resin due to strong suction effect of vacuum.

After manufacturing, the metal mesh on top of the polymer composite is covered by resin. The challenge is to remove some percentage of the resin to let the metal mesh has enough surface to be used for the coating.

3.2. Sandpaper Polishing

Sandpaper is a type of coated abrasive that consists of sheets of paper with grits (commonly, Al_2O_3) glued to one face. Sandpaper exists in a range of grit sizes and is employed for the removal of material from the surface layer and to make the surface rougher. The grit size of sandpaper is inversely related to the particle size. A small number such as 100 indicates coarse grit, whereas a large number such as 600 indicates a finer grit. In this study, as an alternative method to grit-blasting for removal of excessive cured polymer on top of metal wire mesh, exposing it, and providing a rough metallic surface prepared for thermal spray coating, manual sandpaper polishing is tested. As the process is carried out manually, there is no accurate control over the pressure and the speed of polishing. Albeit, it is tried to keep the variable similar for the constant number of passes for each sample.

In this regard, 2.5-2.5 cm^2 coupons of metal mesh/CFRP are cut from the fabricated plate employing a diamond jet. The coupons are manually polished for 30 sec by sliding the top of them on the abrasive side of sandpaper with mesh numbers of 180, 320, and 600. The abrasive side of sandpaper is wetted by water to reduce the friction allowing for polishing of the samples.

Thereafter, the samples were cleaned and characterized to investigate the effect of polishing on the removal of polymer and/or metal wires. This approach is carried out to evaluate the practicality of sandpaper polishing instead of grit-blasting since there are less parameters included in this surface preparation process, and subsequently easier to optimize. Moreover, the parameters such as speed

of polishing, sandpaper grit size, lubricant media, and pressure can be controlled when the process is carried out implementing robotic polishing machines, observable in Figure 3.5 [138].

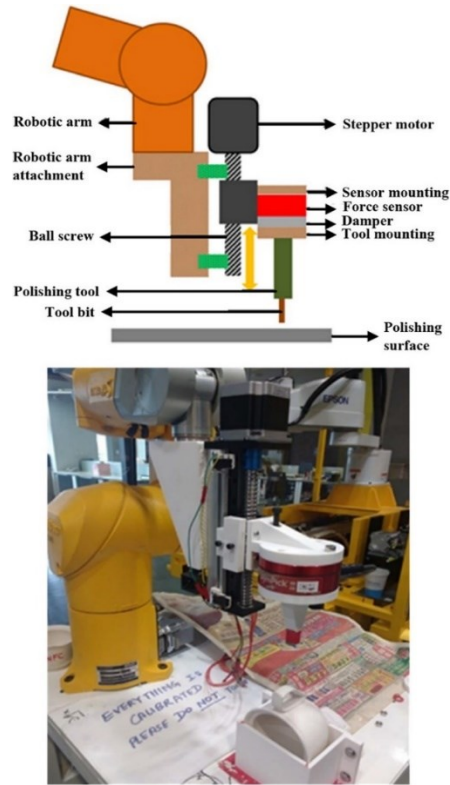


Figure 3.5. A designed and robotic polishing machine [138].

3.3. Grit-Blasting Process

In the present study, aiming for surface preparation, that is optimal removal of polymer and exposure of metal wire mesh on the surface of metal mesh/CFRP, the grit-blasting method is the primary process being evaluated. Similar to the polishing process, metal mesh/CFRP coupons with the dimensions of 3-3 cm² are cut using jet diamonds. The surface pretreatment is carried out in “ECO-420 sandblasting cabinet for light-duty application” located at the Thermal Spray Lab of Concordia University. This cabinet (depicted in Figure 3.6) has a built-in dust collector keeping the processing area free of dust particles, a foot pedal for controlling the flow of the grits,

sandblasting gun, dual side doors, and a large transparent front door, and an air pressure regulator. The specifications of the cabinet are summarized in Table 3.2 as well.

Pursuant to previous studies, Al_2O_3 grits with a mesh size of 80 (particle size of 180 μm) are employed [51], as increasing the particle size could adversely affect the accuracy, and reducing particle size could rise safety concerns by scattering dust and grits out of the cabinet. Moreover, the choice of grit media is based on its availability of it, however, the effect of the abrasive media is further discussed in chapter 4.

The grit-blasting process is carried out both manually and employing an in-house automated setup. The distinguishing difference is that in manual operation, there is no accurate control of the stand-off distance of the blasting gun and sample. Moreover, the blasting time is not being measured precisely and the operator determines the stop of the process based on visualization through the transparent door. This can lead to a high degree of deviation and reduce the repeatability of the process. Moreover, considering an industrial scale, achieving a uniform state of surface preparation is vital, which cannot be easily obtained in manual processing. Especially considering that there are errors such as clogging and sudden unclogging of blasting nozzle causing areas with different surface morphology adjacent to each other. Further, the availability of the grits to get transferred to the nozzle is a challenging issue and the tank should be checked regularly to insure there is enough grit material for the process.

Aside from that, the air pressure regulator allows for grit-blasting with a maximum pressure of 125 psi. However, the highest pressure is considered 100 psi in this study for safety issues. Also, manipulating the blasting gun is important, as the hose transferring the grits to the nozzle is sensitive and wrong positioning can lead to clogging of abrasive media in the hose or its tearing.

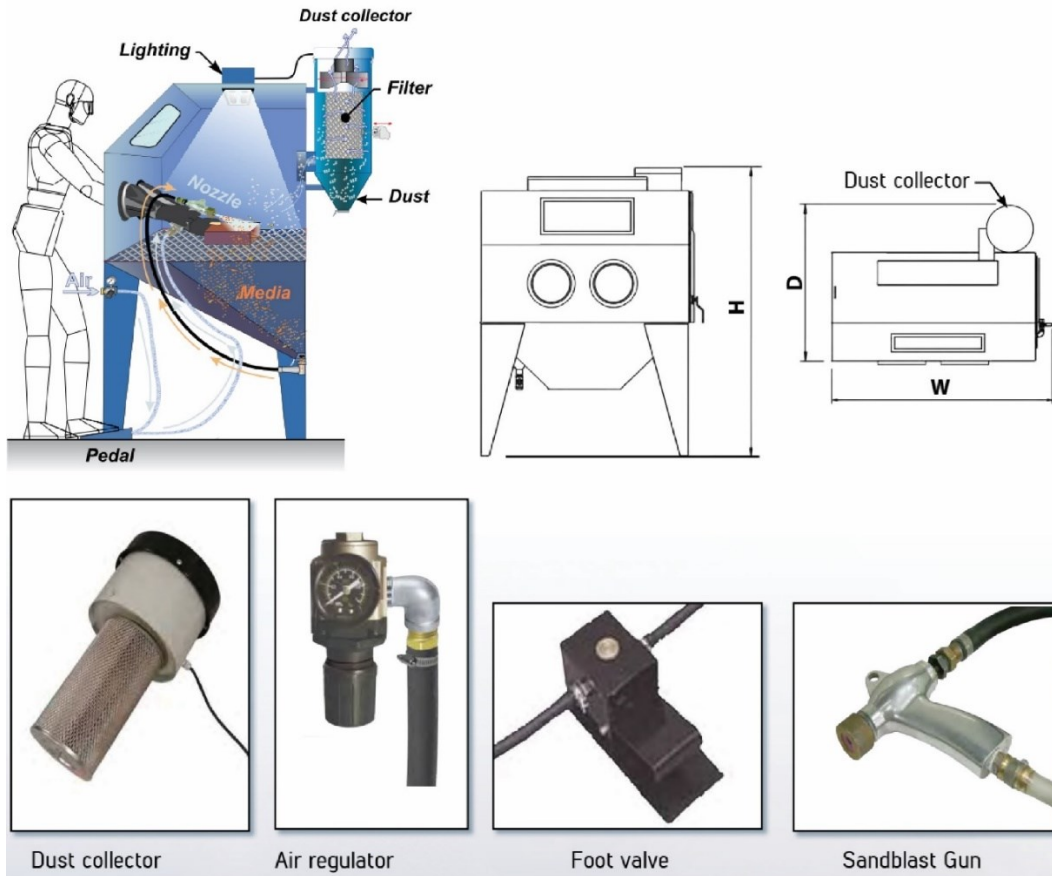


Figure 3.6. Schematic of ECO-420 sandblasting cabinet for light-duty application along with its main components.

Table 3.2. Specifications and dimensions of the ECO-420 sandblasting cabinet.

Parameter	Value
Air requirement	125 psi (max.)
Working area	24 × 22 × 44 in ³
Door opening	19 × 20 in ²
Overall Depth (D)	35 in
Overall Height (H)	65.5 in
Overall Width (W)	53 in

3.4. Automated Grit-Blasting Setup

With respect to the limitations in controlling the parameters of grit-blasting, namely time, stand-off distance and angle, gun movement speed, and blasting pattern in the ECO-420 cabinet, optimizing the manual process would involve a great operational error. Therefore, an automated setup is required enabling control over all the parameters. In this section, the designed fixture is presented illustrating its function and capabilities. Further, measures taken to protect the fixture from abrasive media in the cabinet are explained. Last but not the least, the experiments carried out for the optimization of surface preparation of metal mesh/CFRP employing the automated setup are outlined here.

3.4.1. Design and Assembly

In the manual process, the samples are mounted on a heavy metallic stage and kept fixed in a position. The operator moves the spraying gun across from the sample by hand. However, designing and fabricating a robotic gun holder that can handle the high setback caused by the high blasting pressure is challenging and expensive. Moreover, the size of the grit-blasting chamber and the length of the hose restricts the installation of such a fixture. Considering this issue, a setup is designed that keeps the gun at a fixed position, and the sample mounted on a stage being able to move in two horizontal and vertical directions in the plane perpendicular to the blasting gun. It is vital that the sample holder is capable of bearing the high pressure of blasting and does not collapse during operation. Besides, the setup requires motorized items enabling automation of the system. Aside from that, controlling the setup from outside the cabinet is necessary since the cabinet must be kept closed throughout the processing.

In this regard, two motorized linear actuator stages transverse to each other can provide the passage of the sample in the desired directions. Also, the gun holder can be installed on rails transverse to

the stage allowing for control of the angle and stand-off distance. A schematic view of the initial design is presented in Figure 3.7.

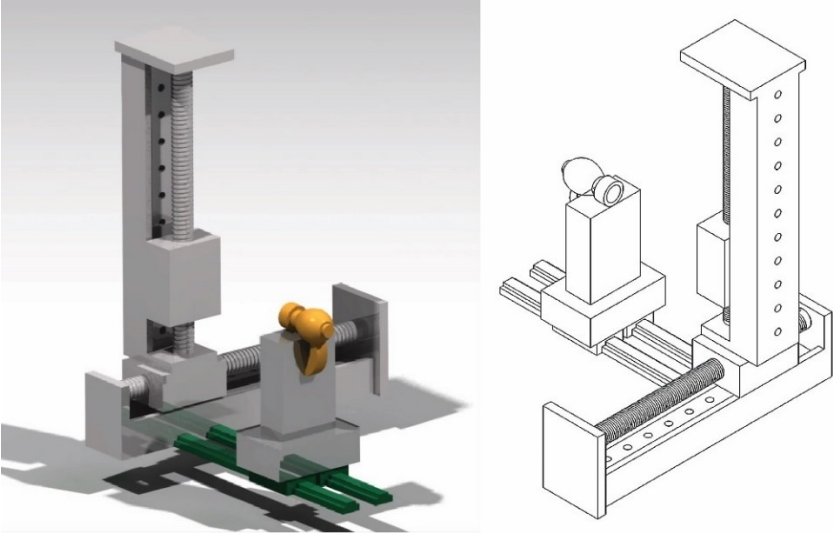


Figure 3.7. Perspective schematic views of the initial designed setup for automated grit-blasting.

For this purpose, RATMMOTOR 100 mm length travel, linear stage actuators equipped with NEMA23 Stepper motors (Figure 3.8) are perpendicularly installed on each other, where the actuators' axes are on the same plane. The selection of this item is dependent on the dimensions criteria of the cabinet. The specifications of the actuators are summarized in Table 3.3.

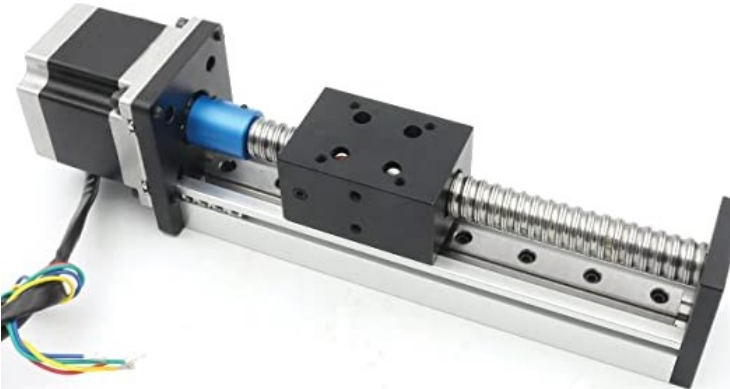


Figure 3.8. The employed linear stage actuators equipped with NEMA23 Stepper motors for the automated setup.

Table 3.3. The specifications of the linear stage actuators and their stepper motors.

Linear Stage Actuator Parameter		Stepper motor Parameter	
Profile width	42 mm	Step angle	1.8 degree
Screw pitch	5 mm		
Accuracy	0.03 mm	Motor flange size	57 mm
Max. speed	50 mm/s		
Horizontal load capacity	30 Kgs	Motor length	56 mm
Vertical load capacity	10Kgs		
Axial load capacity	22Kgs	Holding torque	1.2 N.m

Two MGN12 linear rail guides with a length of 20 cm and MGN12H carriages are positioned in front of the sample stage, parallel to each other. These rails provide controlling the stand-off distance of the gun in a range of 1-21 cm. However, it is important to have a minimum stand-off distance limit avoiding the bounce back of blasting media to the stream and lowering blasting action. Also, this can lead to the wear of the gun and cabinet. As for the gun holder, an adjustable pipe bracket (adjustable in the range of 5-10 cm) is installed on the carriages. Indeed, the adjustability feature can provide control over the angle of blasting. The strap is able to fasten a cylindrical tube (similar to the head of the gun) with a diameter of 2.5-3.75 cm. Despite that, rubber inserts are used between the body of the gun, and the clamp not only better fixes the gun, but also protects it from scratch.

The stepper motors of actuators should be programmed to provide the passage of the samples with a pattern similar to the manual one, presented in Figure 3.9.

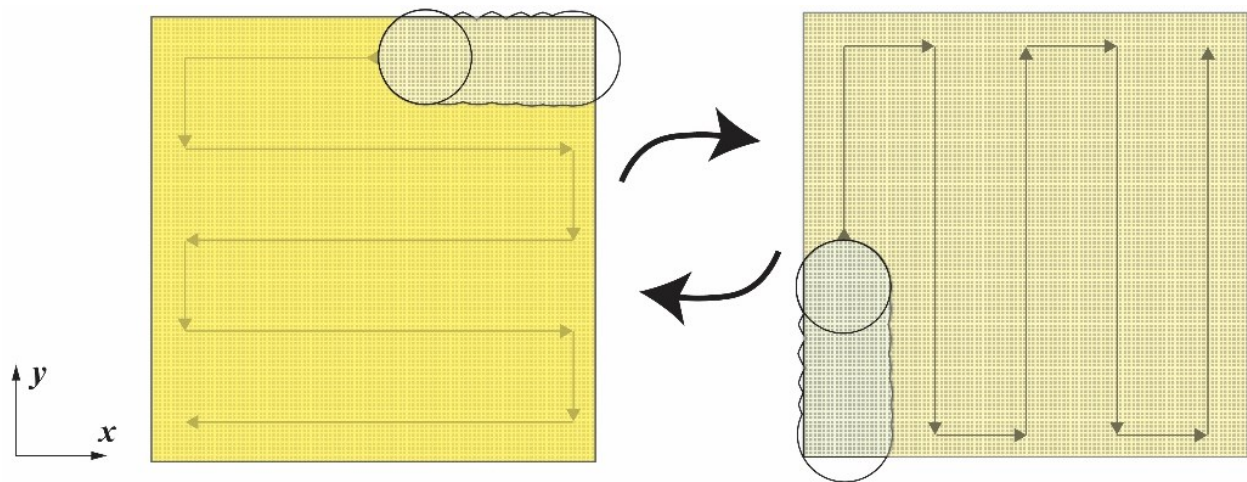


Figure 3.9. The pattern of grit-blasting and movement of the stage in front of the grit-blasting gun as a loop starting with the left image.

This way it is possible to control the speed of grit-blasting, the number of passes, and to ascertain uniform processing of all the sample areas. In this regard, TB6600 micro stepping drivers, ensuring low vibration and high efficiency, are programmed by an Arduino Uno kit, and powered by a 24 V power supply AC/DC adapter. The wiring of each component is illustrated in Figure 3.10.

In addition, the Arduino kit realized the employment of LCD and IR modules for establishing remote control on the fixture from outside the blasting cabinet. The wiring schematic of these modules is presented in Figure 3.11. The programming of the microcontroller will be further discussed in the next section. An image from the assembled setup is depicted in Figure 3.12.

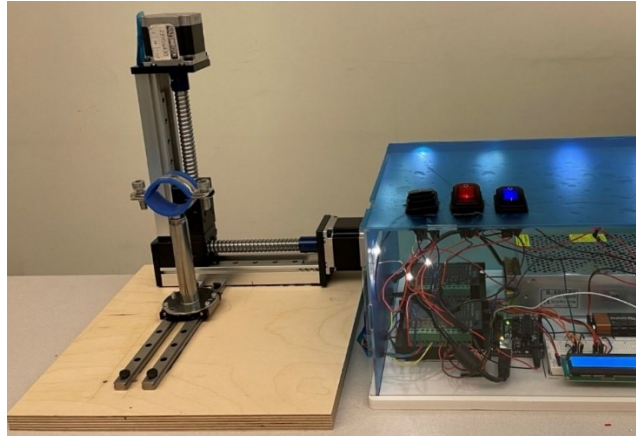


Figure 3.12. A view of the assembled automated grit-blasting setup.

3.4.2. Programming & Features

The Arduino open-source platform is a versatile tool, yet simple interface for the combination of software and hardware. The board can be connected to a computer via USB, where it can be programmed with the Arduino integrated development environment (IDE). The microcontroller executes the uploaded program interacting with inputs such as IR remote controller and outputs such as LCD and motors. The Arduino codes are written in C++ programming language and comprised of special functions and methodology. The human-readable code is then compiled by IDE to machine language, being uploaded to the board's memory. Moreover, the serial monitor of the IDE is an invaluable asset for debugging the code and screening the real-time performance of the board. The developed Arduino code in this study includes four primary parts; that is setup, input, data manipulation, and output. In the following of this section, it is tried to elucidate each part of the code in a comprehensive manner.

3.4.2.1. Code Setup

At first, including the required libraries in the IDE is an essential step. For this purpose, the *include* command is utilized to add three libraries of *IRremote.h*, *LiquidCrystal.h*, and *AccelStepper.h* are

responsible for the transmission of data to/from IR receiver, LCD, and stepper motors, respectively. Thereafter, the constant and variable parameters, including time, are defined. Additionally, the pins on the Arduino board are defined based on the wiring of components and the corresponding role of the wire. In this regard, six pins are introduced for the LCD as for its register select for memorizing the data on the chipset, the enabling pin, and four pins for transmission of data in 4-bit mode. Besides, one pin is registered for the IR receiver, which is responsible for receiving signals from the remote controller and decoding them into comprehensible data. Also, two stepper motors are defined, each with two pins for controlling the rotation direction and speed. An essential part of the code regarding the stepper motors, especially when employing *AccelStepper.h* library, is to set the stepper motors' acceleration and maximum speed. In the case of acceleration, the value is set to 25 mm/s², and for the speed the maximum possible speed of 50 mm/s. However, the speed parameter is then limited to 7 mm/s since the actuator length is small and high speeds cannot be reached easily. Also, such high speeds are not the case in this study.

3.4.2.2. Input

After setting up all the components in the code and making sure they are running and controllable, the code requires input for processing and controlling the components. The main inputs for this study are the movement and speed of the stepper motors, as well as the number of loops. All the inputs can be fed into the board through either IR remote controller or using the keyboard of the connected computer to the board. In each case, the dimensions of the sample (in the range of 10-50 mm), speed of the motors (in the range of 3-7 mm/s), and the number of blasting loops (in the range of 1-10) must be provided. In this scenario, the LCD shows the inserted values to facilitate

communication with the board. It is worthwhile of mentioning that this process is done in a loop where the data are stored in arrays and will be further used for the data manipulation part.

3.4.2.3. Computation and Output

The computational part of the developed code is regarding the transformation of input dimensions and speed to the number of steps that the stepper motors must take to reach the destined locations. Considering the x and y coordinates of the sample are lower than the nozzle axis, the motors move the stage so that the sample's top-right corner gets aligned to the blasting axis. Afterward, the vertical and horizontal motors will run sequentially with the defined speed, to achieve the pattern of figure 3.9. At the same time, the LCD provides blasting time. By finishing the loop, the LCDs demand stopping the blasting, and the motors bring the stage to its home position after a short delay.

3.4.3. Protection and Safety

With respect to the high pressure of the blasting, it is vital to assure the strength of the actuators against bending. Considering the geometry and applied forces on the fixture, the bending moment stress has the most pronounced effect, which can lead to collapse and failure of the actuators during the blasting process. Therefore, to increase the second moment of inertia and ensure a safe processing condition, the setup is installed on a wooden plate avoiding the collapse of the parts. This way, despite increasing the second moment of inertia, the gun weight and the blasting reaction force is being applied to the wooden plate contributing to fixing the setup and avoiding accident.

Another crucial criterion in designing the automated grit-blasting setup is the protection of the mechanical components of the fixture from the abrasive media in the cabinet. To illustrate, the grits being propelled by high pressure are harmful to the mechanical parts such as the actuators'

body, the stepper motors, and the sample stage. Moreover, the fluctuation of the grit particles in the cabinet, due to the air flow caused by the suction mechanism, can lead the particles under the carriage seal and hinder the bearing balls, which causes the carriage to fully stick in the position. Therefore, the fixture must be protected by employing erosion-resistant films. A potential tool in this regard is vinyl stencil films commonly used in artistic crafts for creating a pattern or graphical design on a part of an item using low-pressure blasting while protecting the other parts of the item.

In order to ascertain the functionality of stencil vinyl film, 5 sheets of protective films containing 1 to 5 layers of vinyl films are tested under direct grit-blasting with high pressure of 100 psi and an estimated stand-off distance of 6 cm for quite a long time. It is observed that a single layer of the vinyl film would not get eroded easily under the condition but gets deformed. However, in the cases of 3 or more layers, even the deformation would be minimal. Thus, it is determined to employ at least 4 layers of vinyl film to ensure the protection of the setup for a long period of time.

More importantly, it is extremely vital to avoid contact with the vinyl film to the actuators. It is due to the static electricity caused by the friction of erosive particles on the protective film, which causes a voltage difference and interrupts the function of stepper motors. To do so, at first, thick nylon (vacuum bag) is applied to the fixture protecting the rails from the suspended particles. Then two sheets of 6 mm thick plexiglass are installed on the front and back of the vertical actuator stage enabling a flat, stiff surface for the application of the protective vinyl film. Thereafter, 4 layers of vinyl films are applied on the front plexiglass protecting the fixture against propelled particles from the nozzle. The nylon is also installed on the gun holder rails protecting them from dust and particles. In addition, three power switches are employed enabling emergency stops of the motors by breaking the circuit separately for motors, microcontroller, and lightning system.

3.4.4. Design of Experiment

There are several parameters required to be analyzed in grit-blasting processes. Thus, it is highly important to select the most influential ones and their levels, prior to carrying out the processing. The optimization can be done using statistical design techniques with a reduced number of experimental runs or iterations. Also, the statistical design methods reassure the systematic study of the variables that affect the surface preparation state. Design of experiments (DOE) using Taguchi factorial design is a common statistical technique. This approach includes a matrix of selected variables versus a series of experimental runs. The variables determine the matrix size and number of runs. In another word, an experiment aims for the prediction of the outcome by making a change on the variables, which is denoted by independent variables. The variation in the independent variables is assumed to result in a variation in outcomes, also known as dependent variables. To estimate the magnitude of variable effect on grit-blasting state and to regulate which parameters affect this state significantly, an analysis of variance (ANOVA) is performed to obtain regression models for predicting the response at other levels of independent variables.

In this study, three independent variables, that can be well controlled during processing, are selected, namely, blasting pressure (P), stand-off distance (d), and blasting time (t). Each variable is studied at three different levels to assure if they pose a linear or non-linear effect on the response since selecting two levels will result in a linear effect, which can lead to an unpredictable error in the regression model. Pursuant to previous studies, grit-blasting with a pressure of 76 psi and a distance of 6 cm for 150 sec was the initial experiment [18]. However, due to the variability of the results, it is attempted to investigate the effect of P , d , and t on the exposure level of wires. In this regard, each parameter is studied at three different of levels of $P = 60, 80, 100$ psi, $d = 7, 10, 13$ cm, and $t = 60, 120, 180$ sec. The complete set of designed tests containing 27 runs is highlighted

in Table 3.4. These values are determined based on trial and error and considering the safety issues regarding maximum P , as explained previously.

Table 3.4. the parameter sets of design of experiment testing for analysis and optimization of grit-blasting process for metal mesh/CFRP system.

sample	Pressure (psi)	distance (cm)	time (sec)
1	60	7	60
2	60	7	120
3	60	7	180
4	60	10	60
5	60	10	120
6	60	10	180
7	60	13	60
8	60	13	120
9	60	13	180
10	80	7	60
11	80	7	120
12	80	7	180
13	80	10	60
14	80	10	120
15	80	10	180
16	80	13	60
17	80	13	120
18	80	13	180
19	100	7	60
20	100	7	120
21	100	7	180
22	100	10	60
23	100	10	120
24	100	10	180
25	100	13	60
26	100	13	120
27	100	13	180

With respect to the fact that a quantitative response is required for the statistical analysis of variables, a feature must be extracted from the surface of grit-blasted samples. Sample thickness and weight are not proper choices, since there is a high variation between samples themselves, and accurate measurement of these features is difficult and requires special equipment due to the small size of coupons. Moreover, they are not reflecting a good resolution for an industrial setup, or large-scale components. Therefore, the level of mesh exposure, which is an essential parameter for the coating process, is targeted as the response of the system. For this purpose, characterization of the cross-section of as-fabricated samples and the top surface of grit-blasted samples inspired the idea of correlating the length of exposed wires to the resin removal height and calculating the metal mesh exposure level with respect to fully resin-covered metal mesh. It is found that the thickness of the metal mesh/resin top layer in the as-fabricated sample is 120 μm , which is less than the metal mesh. It is mainly due to the flexible pattern of the selected metal mesh, which is slightly compressed under the pressure during the fabrication process because of the caul plate and autoclave pressure. This is further verified by a micrometer, where the value reached 120 μm from 124 μm by tightening the gauge and inserting extra force.

Considering the pattern and dimensions of the metal mesh (Figure 3.13), a polynomial can be fitted on the metal wires, where it correlates the length of exposed wire observed from the top view to the height of metal exposed and not covered by the resin. For this purpose, ImageJ software is utilized to extract the coordination of several points on the wire in a cross-sectional view of the system on an optical microscopy image. The coordination is then implemented for interpolation of the curve as:

$$h = 108.77\left(\frac{x}{2}\right)^4 - 58.608\left(\frac{x}{2}\right)^3 + 8.495\left(\frac{x}{2}\right)^2 - 0.067\left(\frac{x}{2}\right) + 0.06$$

where h is the average height of exposed wires and x denotes the average length of them. It is worthwhile to mention that ideally, where the metal wire mesh displays exact dimensions with no disorder, the maximum value of x would be L_c , providing less than 50% exposure level. It is also important to consider the employed metal mesh displays a complex twill weave pattern, where one wire alternatively passes from above and bottom of two wires, while the wires next to it just pass one. The latter wires display lower height and get exposed in a longer processing time.

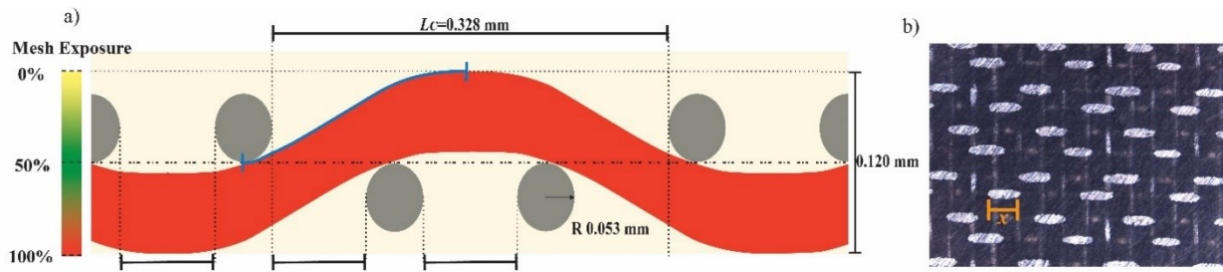


Figure 3.13. a) a schematic of the cross-section of resin-covered metal mesh in the metal mesh/CFRP system in the ideal condition revealing the dimensional characteristic and an approximate measure for mesh exposure. b) a top view optical microscope image of sandpaper polished coupon demonstrating exposure of metal wires and its dependency to cross-sectional view.

3.5. Characterization

3.5.1. Portable Digital Microscopy

A major innovation of this study is the application of small, affordable, portable digital microscopy for the characterization of grit-blasted metal mesh/CFRP systems. For the purpose of characterization from the top view, “Skybasic handheld digital microscope” is utilized providing high-resolution images with a magnification of 50-1000. The microscope is equipped with 8 LEDs providing the light, the intensity of which can be controlled. This feature can be utilized to achieve a distinguishable contrast between metal and polymer, as they pose different light reflection indexes. In the current study, the microscopy process is conducted by employing an adjustable

stand holder allowing for obtaining images with the same magnification and quality. Figure 3.14 demonstrates the setup of the digital microscopy characterization and the microscope stand. It is worthwhile of mentioning that the microscope is also equipped with a Wi-Fi kit providing the capability of real-time analysis by mobile phones and tablets as well.

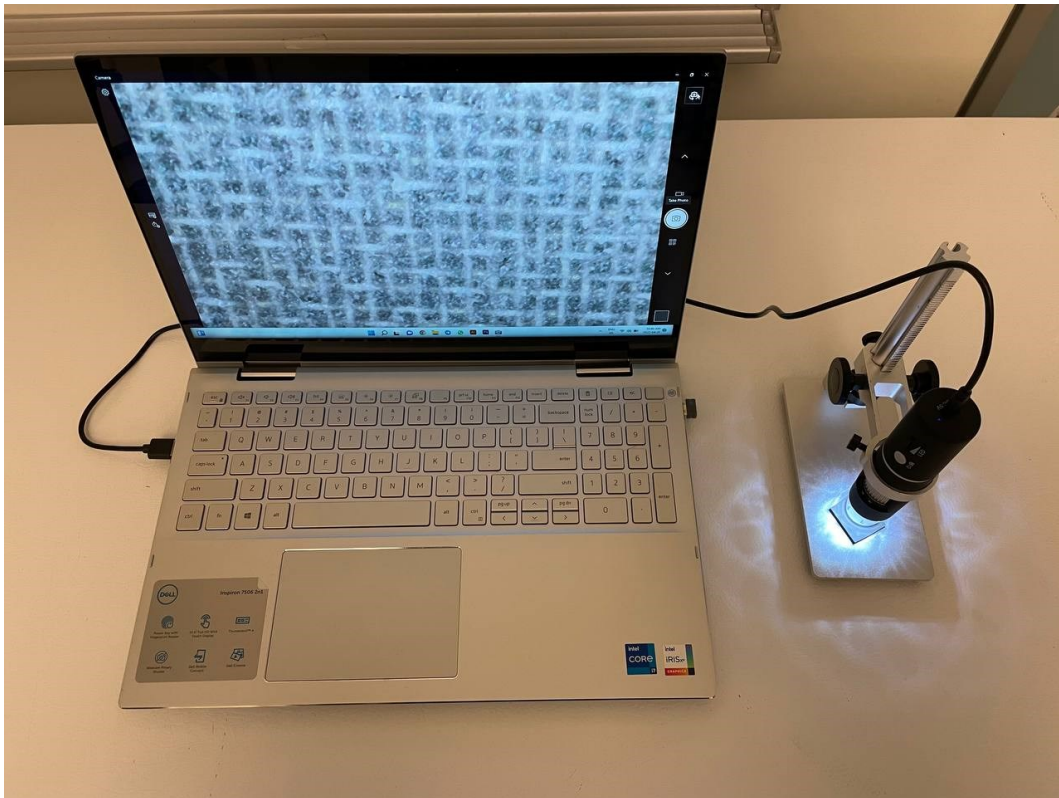


Figure 3.14. A view of the characterization utilizing a portable digital microscope.

3.5.2. Optical Microscopy

The optical microscope, also known as the light optical microscope, uses visible light and a sequence of lenses enabling magnification of images from small samples. Basic optical microscopes are simple; however, more complex designs are developed to improve resolution and sample contrast.

The image from an optical microscope can be captured by normal light-sensitive cameras to generate a micrograph. Employment of metal-oxide-semiconductor and charge-coupled device cameras allows capturing of digital images [139]. Figure 3.15 depicts a schematic of an optical microscope equipped with a digital camera enabling examination of samples by showing the image directly on a computer screen.

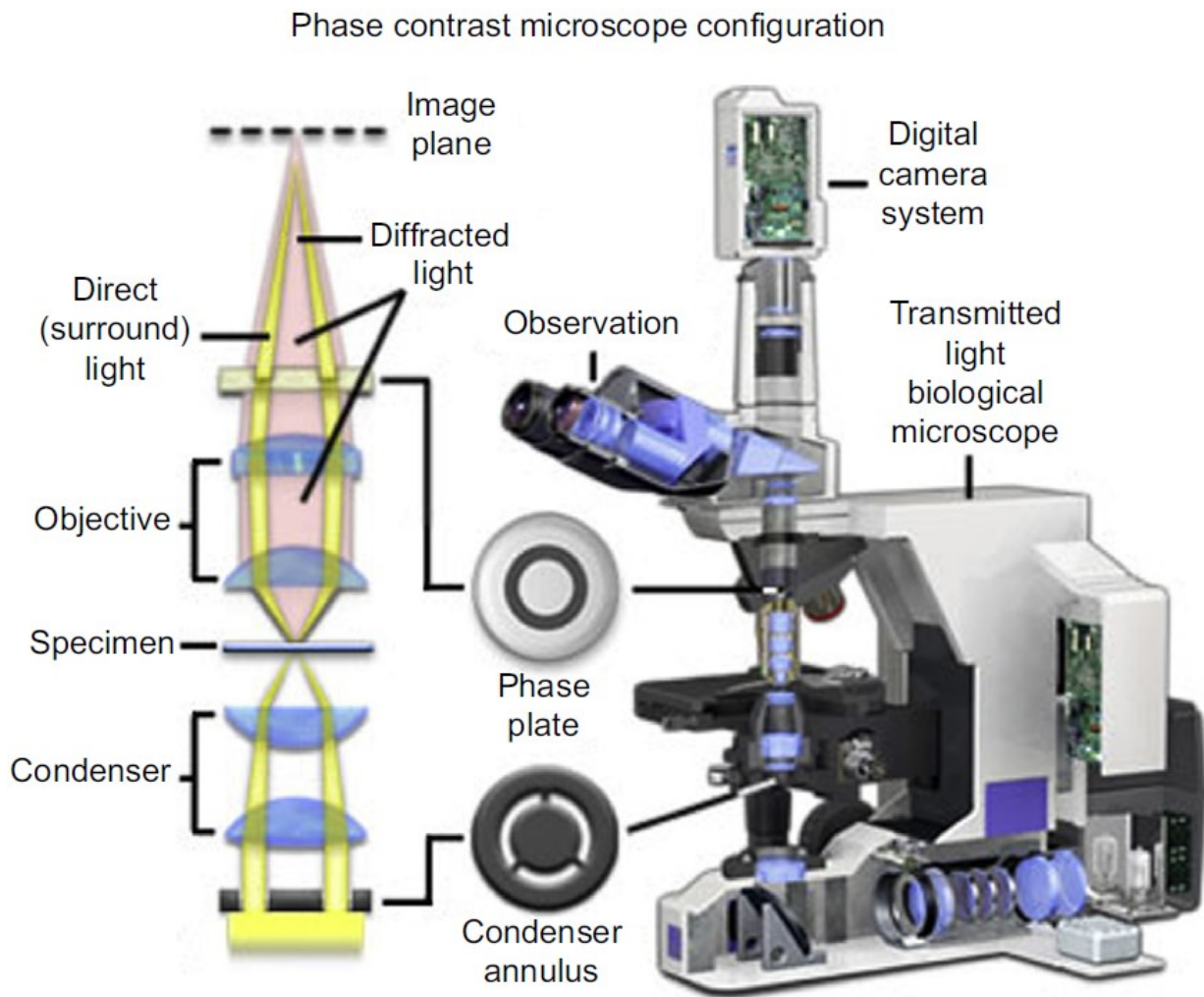


Figure 3.15. A schematic of an optical light microscope, its components, and working principle [139].

In this study, optical microscopy is employed to further characterize the grit-blasted samples and validate the results obtained by digital microscopy. For this purpose, the samples are cut in half

using a diamond jet. Thereafter, they are mounted in an epoxy curable at low temperature (Figure 3.16). This step is primarily done to facilitate the polishing of the cross-section of the sample to obtain an even surface, due to the limited depth of view of the optical microscope.

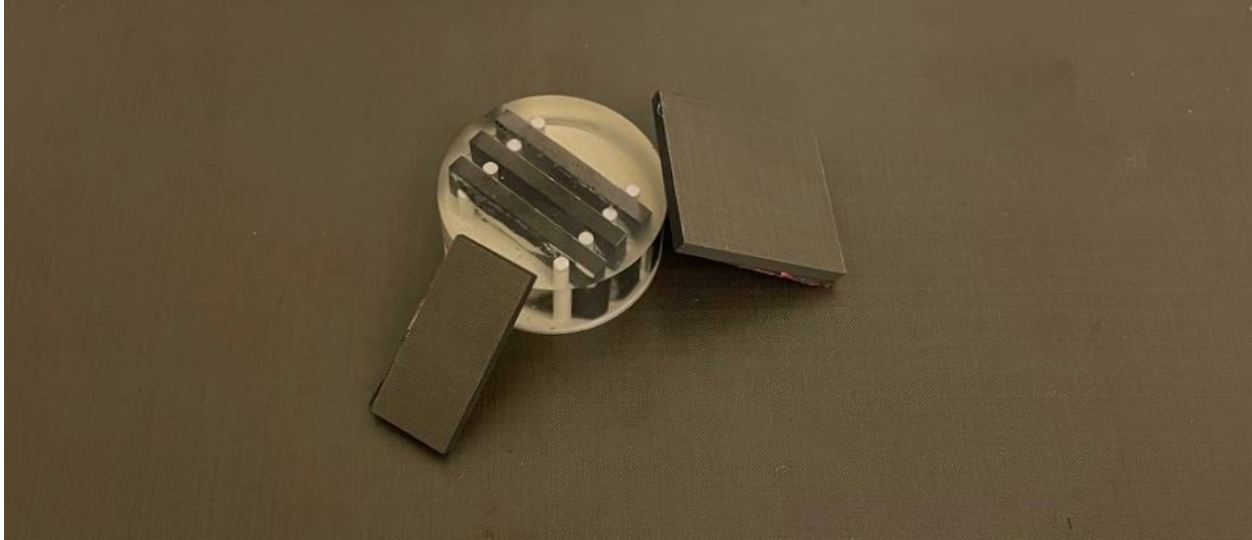


Figure 3.16. An image of the coupons prepared for grit-blasting, sample cut in half, and samples mounted for polishing and characterization by optical microscope.

3.5.3. Roughness Measurement

As it has been previously discussed, other than the exposure level of metal mesh in the thermal spray coating of metal mesh/FRPC, surface roughness plays a crucial role in coatability and coating properties. Therefore, this parameter can be considered as another response of the system for analysis and optimization of surface preparation process parameters, i.e., grit-blasting. In this regard, the surface roughness of the samples is evaluated using a profilometer. A Mitutoyo SJ 210 profilometer with a standard detector (Figure 3.17) is utilized, where the stylus (contact detector) is moved across the sample measuring the surface variation based on its vertical displacement. Indeed, the contact surface roughness measurement is advantageous in this case since it is not dependent on the surface reflectance or color.



Figure 3.17. Mitutoyo SJ 210 profilometer.

Chapter 4: Results and Discussion

In this chapter, the result of the image analysis carried out on the grit-blasted metal mesh incorporated polymer composites is presented discussing the effect of each processing parameter. Moreover, a quantitative model has been suggested for the prediction of metal mesh exposure levels as a roadmap for future work.

4.1. The Effect of Sandpaper polishing

As mentioned previously, sandpaper polishing of metal mesh/CFRP is carried out employing SiC sandpaper with various coarseness and polishing times in order to evaluate the capability of this method for the preparation of the substrate for the thermal spray coating process. The optical microscopy images of the polished samples are shown in Figure 4.1.

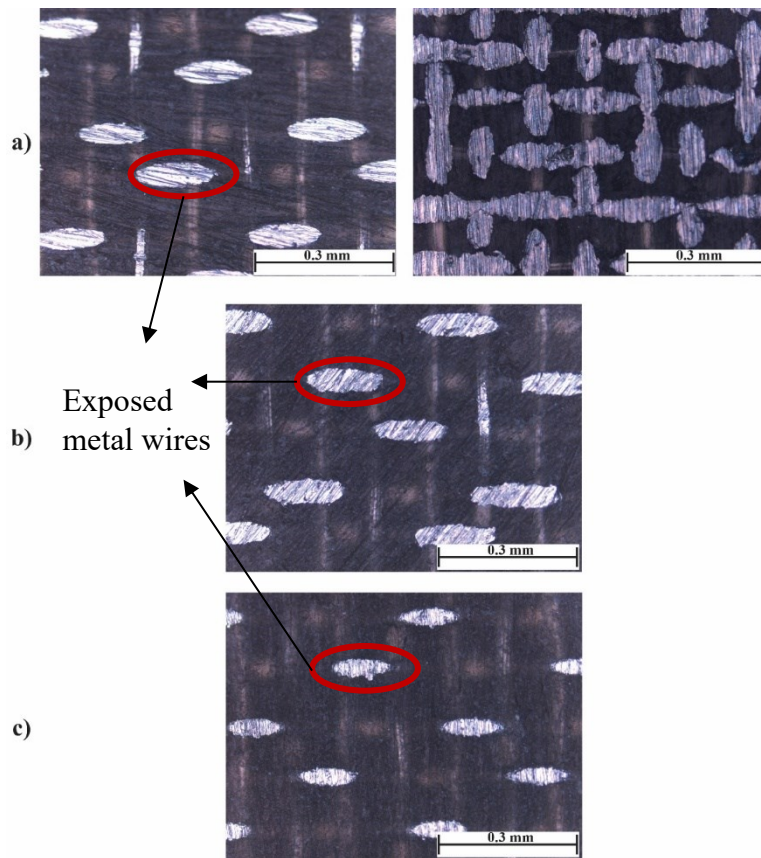


Figure 4.1. Optical microscope images of polished samples with sandpaper of a) 180, b) 320, c) 600.

As it can be observed, increasing the sandpaper number (reducing particle size) leads to a lower abrasion effect, and obtaining a finer surface. Generally, the polishing process causes the removal of metal mesh and resin simultaneously leading to a fine surface with lower roughness in comparison to grit-blasted ones. Moreover, the surface of metal wires gets slightly exposed while being surrounded by polymer from the sides. At the same time, the wires are deformed and distributed on the surface when the processing time increases. However, this pattern is only on the surface layer of the wires and is not in-depth. Therefore, it can be concluded that, although the availability of metal on the surface increases due to superficial deformation of wires, the low surface roughness and lack of in-depth metallic support below the deformed areas can cause the failure of the part under the coating process.

To enhance the roughness, a light grit-blasting process can be carried out, but it can lead to abrasion of the deformed areas and lower the availability of the metal. Another possible resolution can be the employment of finer metal mesh (e.g., mesh size of 400), where the open area of the mesh is smaller, and wires are closer to each other. This way the deformation and distribution of two neighboring wires can superpose and create a thicker metallic area in the open areas, which is then coatable. This is to be tested and evaluated along with a coating of the as-polished samples (with a metal mesh of 200) to validate the statement above.

Up to now, grit-blasting has been the only surface treatment technique carried out for preparing metal mesh/FRPCs prior to coating. In this regard, devising alternative techniques, as well as modifying and optimizing grit-blasting is of high importance. In the next sections, the results of the grit-blasting process are comprehensively studied.

4.2. The Effect of Grit-blasting

As indicated, the grit-blasting process is the primary technique for the preparation of metal mesh/FRPCs for the thermal spraying process. In this section, the result of grit-blasting utilizing an automated setup is presented to study and analyze the effect of grit-blasting parameters on metal mesh exposure and the preparation state of the system.

4.2.1. Visual Inspection

Visual inspection, however dependent on eyesight, is a rudimentary step in evaluating the surface preparation state of the grit-blasted samples. Figure 4.2, Figure 4.3, Figure 4.4 show the grit-blasted samples under the pressure of 60, 80, and 100 psi, respectively.

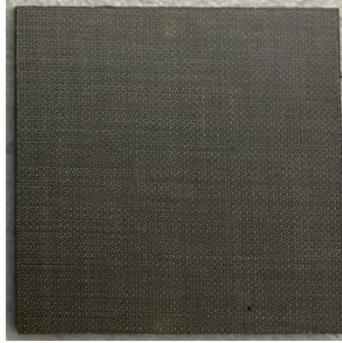
The very fundamental feature that is noticeable in all the grit-blasted samples is their color and reflection. The as-fabricated samples are dark and matt, in contrast to the grit-blasted samples, which are shinier. The most exquisite reason is the removal of polymer from the surface and exposure of metal wires, which reflect the light. In the same scene, it must be noticed that the grit-blasting parameters affect the surface roughness. Considering the fact that light reflection is a function of surface roughness as well, the reflection from samples is different.

Moreover, the state of grit-blasting can be roughly estimated based on visual inspection. In the case of under-blasted samples, the color of the sample is comparatively darker. The over-blasted samples are easily distinguishable as the metal mesh is removed and the black CFRP is exposed (i.e., samples 12, 15, 19, 20, 21, 23, and 24). However, this is not a precise measure, and a more detailed analysis is required to inspect the metal mesh exposure and state of preparation.

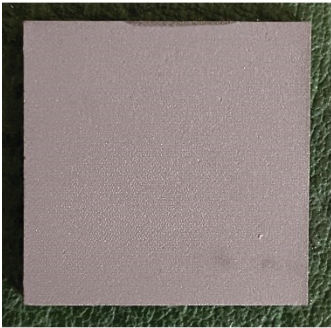


Figure 4.2. Images of samples 1-9 (grit-blasted under the pressure of 60 psi) in comparison to the as-fabricated state utilized for visual inspection.

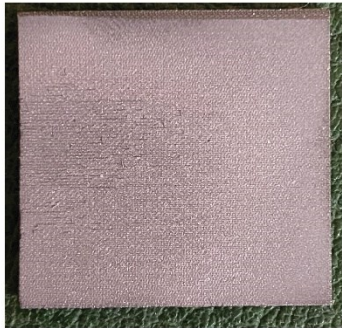
As-fabricated



10



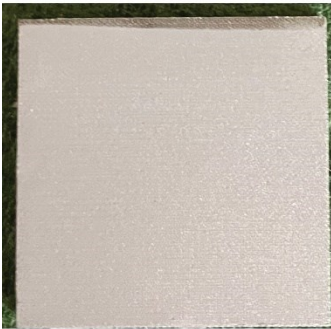
11



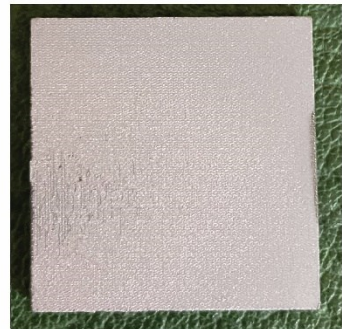
12



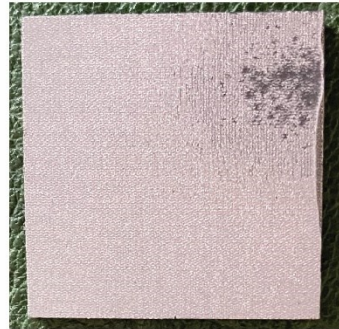
13



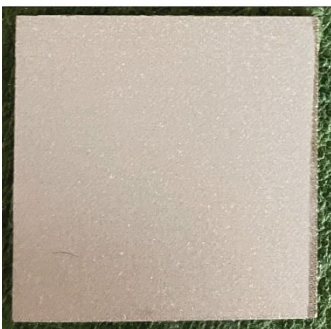
14



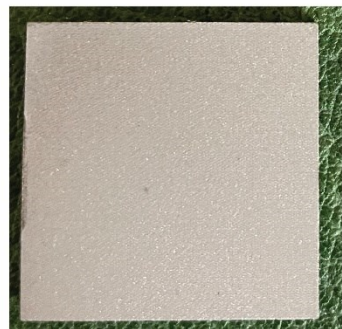
15



16



17

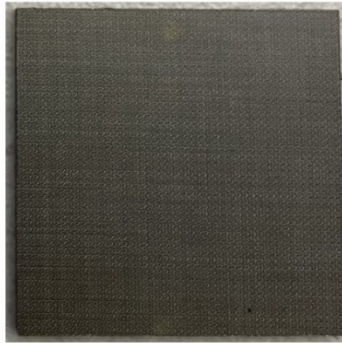


18



Figure 4.3. Images of samples 10-18 (grit-blasted under the pressure of 80 psi) in comparison to the as-fabricated state utilized for visual inspection.

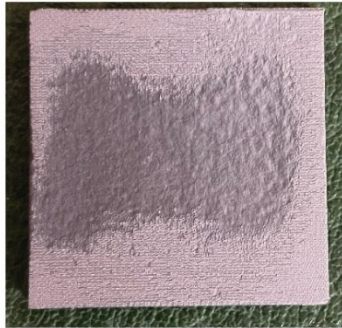
As-fabricated



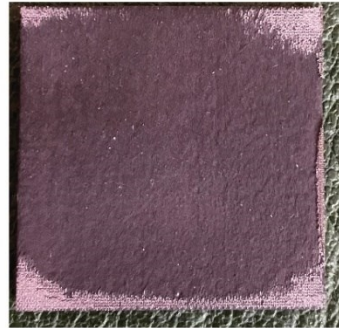
19



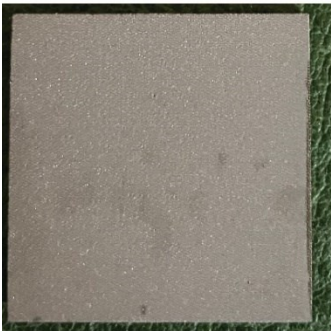
20



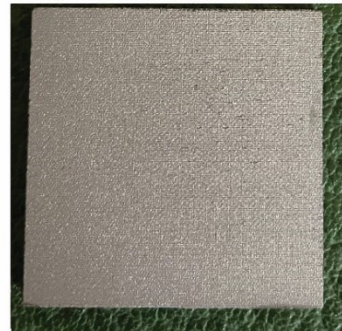
21



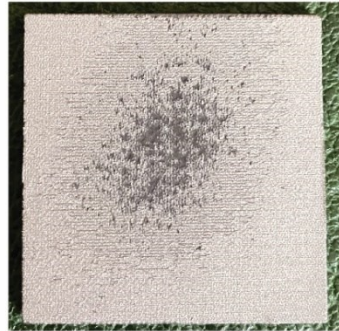
22



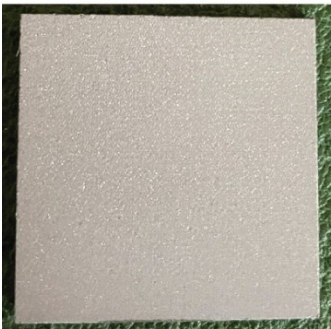
23



24



25



26



27

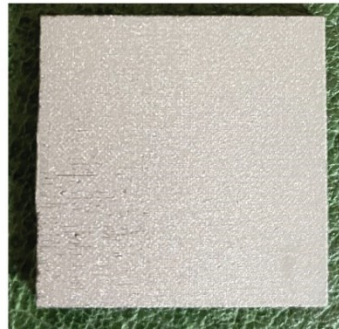


Figure 4.4. Images of samples 19-27 (grit-blasted under the pressure of 100 psi) in comparison to the as-fabricated state utilized for visual inspection.

4.2.2. Digital Microscopy Inspection

In order to overcome the limitation of eyesight in visual inspection, and comprehensively study the effect of grit-blasting parameters, microscopy of the grit-blasted samples is essential. Moreover, aiming to develop an evaluation method in a non-destructive manner, portable digital microscopy is utilized. The microscopy images from 5 random areas of grit-blasted samples are implemented for analyzing and measuring the average metal wire exposure length in each sample. The measurement is done with ImageJ software, where lines were manually plotted on exposed wires, and the software calculated the length of each wire based on the number of pixels and the defined pixel-length ratio. Figure 4.5 Figure 4.13 display the microscopy image of samples along with the corresponding distribution of wire length exposure. The samples are categorized based on the grit-blasting pressure and stand-off distance into 9 groups.

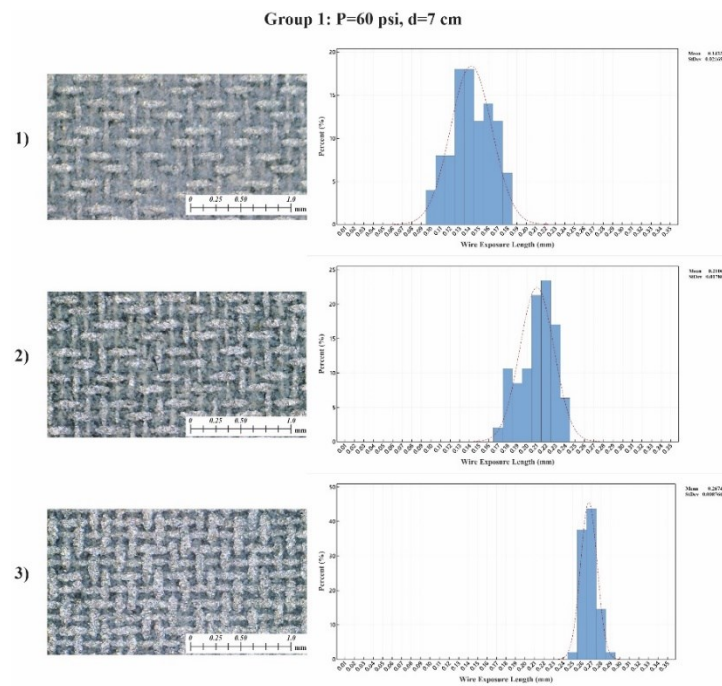


Figure 4.5. Digital microscope images of samples 1-3 (grit-blasted under P=60 psi with d= 7cm), along with their corresponding distribution of metal wire exposure length.

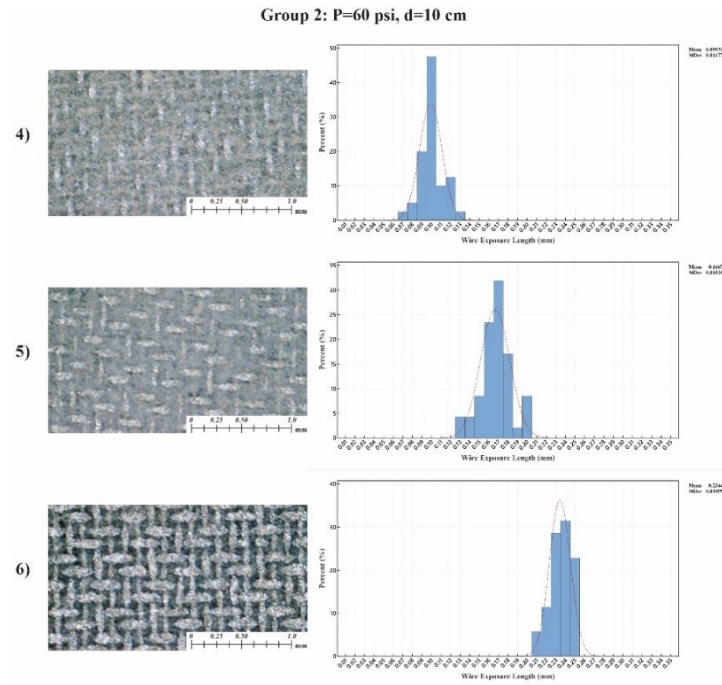


Figure 4.6. Digital microscope images of samples 4-6 (grit-blasted under P=60 psi with d= 10cm), along with their corresponding distribution of metal wire exposure length.

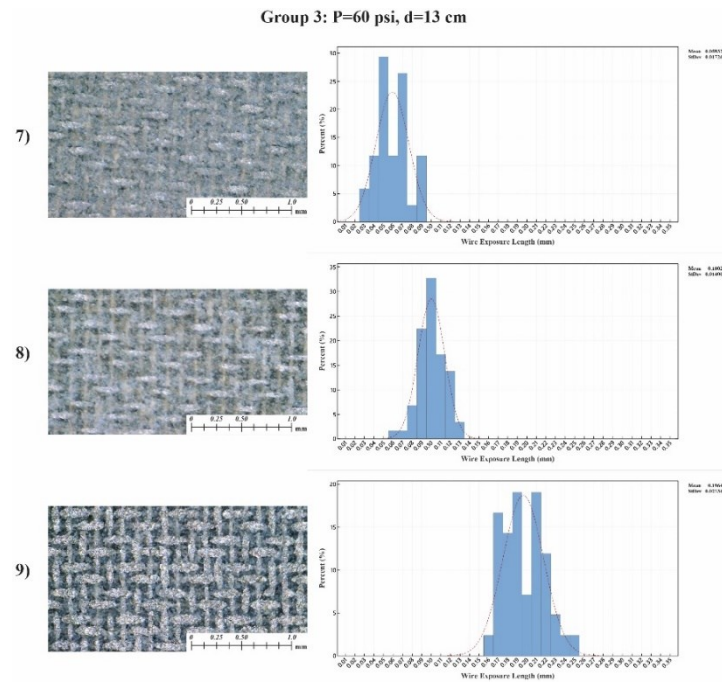


Figure 4.7. Digital microscope images of samples 7-9 (grit-blasted under P=60 psi with d= 13cm), along with their corresponding distribution of metal wire exposure length.

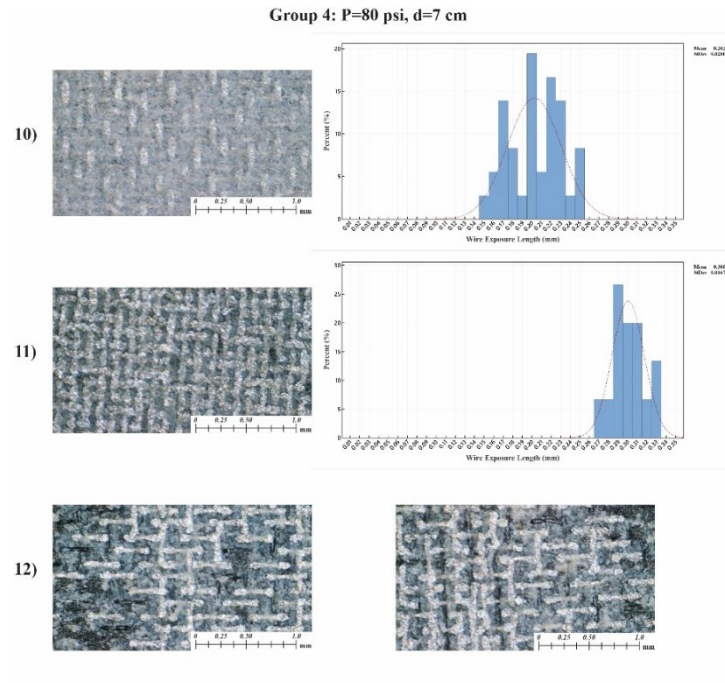


Figure 4.8. Digital microscope images of samples 10-12 (grit-blasted under P=80 psi with d= 7cm), along with their corresponding distribution of metal wire exposure length.

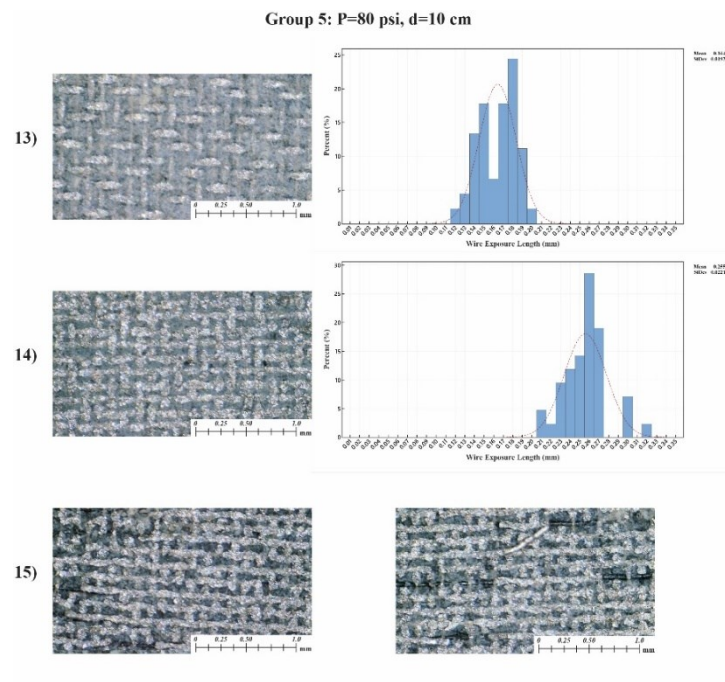


Figure 4.9. Digital microscope images of samples 13-15 (grit-blasted under P=80 psi with d= 10cm), along with their corresponding distribution of metal wire exposure length.

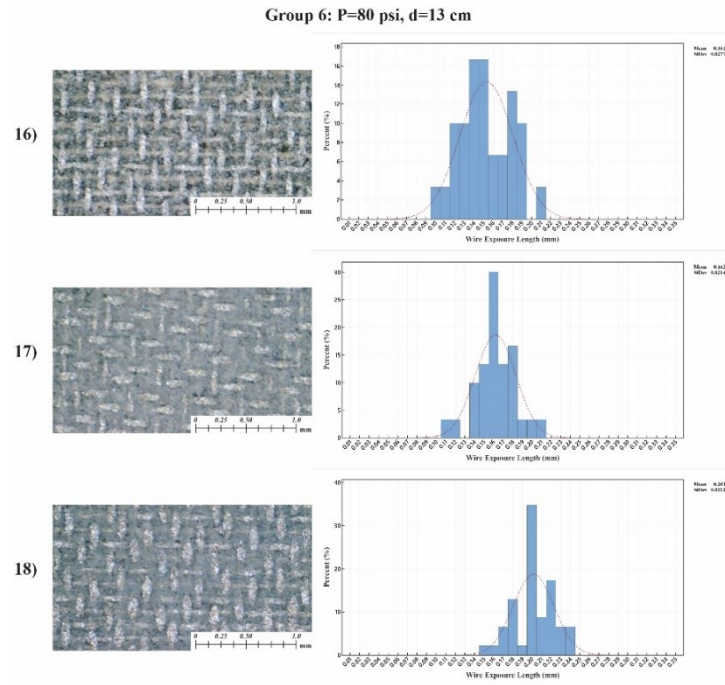


Figure 4.10. Digital microscope images of samples 16-18 (grit-blasted under P=80 psi with d= 13cm), along with their corresponding distribution of metal wire exposure length.

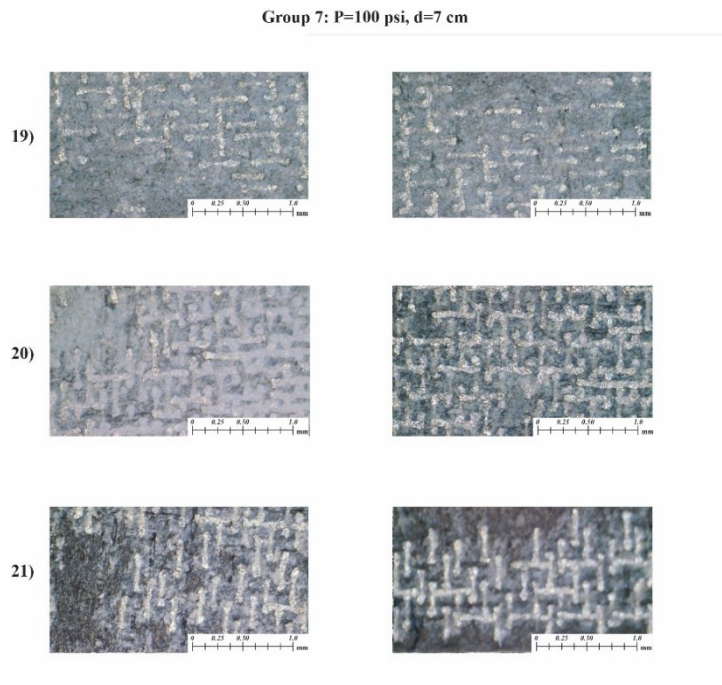


Figure 4.11. Digital microscope images of samples 19-21 (grit-blasted under P=100 psi with d= 7cm), along with their corresponding distribution of metal wire exposure length.

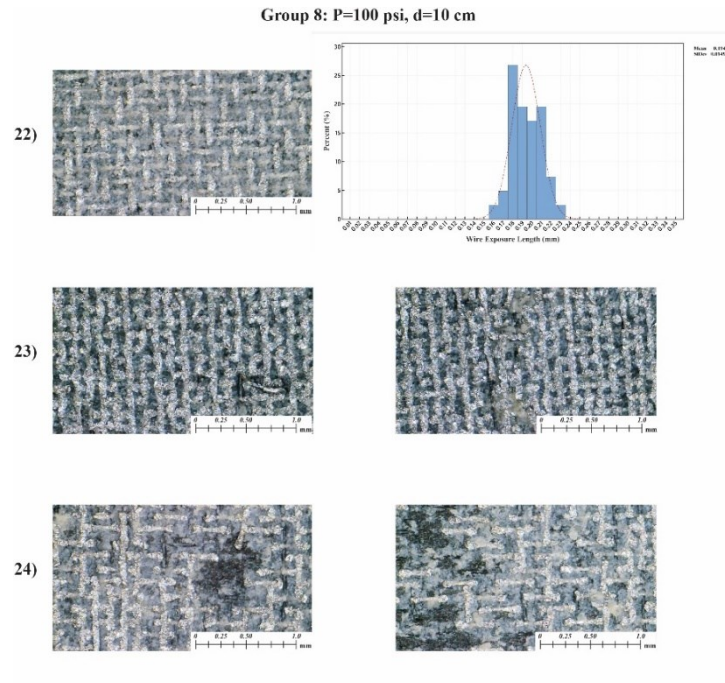


Figure 4.12. Digital microscope images of samples 22-24 (grit-blasted under P=100 psi with d= 10cm), along with their corresponding distribution of metal wire exposure length.

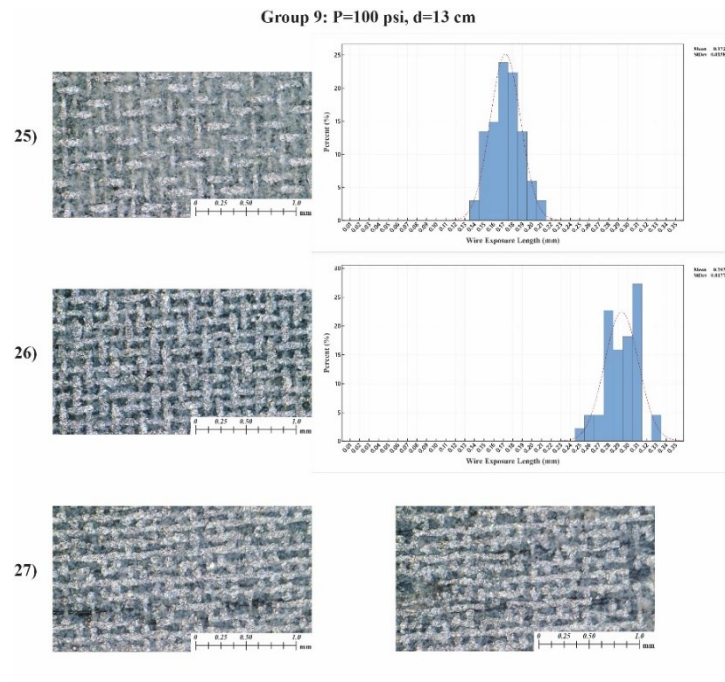


Figure 4.13. Digital microscope images of samples 25-27 (grit-blasted under P=100 psi with d= 13cm), along with their corresponding distribution of metal wire exposure length.

In order to extract the average metal wire exposure length, five microscopy images from random areas of each sample are analyzed employing ImageJ software. First, employing the calibration tool, the pixel-to-length ratio is determined. Then, lines are drawn manually on the exposed wires measuring the number of pixels the line covers and transforming it to the corresponding length. The corresponding distribution of metal wire exposure length for each sample is plotted in Figure 4.5Figure 4.13 as well. It is worthwhile of mentioning that in the case of over-blasted samples, the exposure length cannot be obtained due to either complete removal of metal wire or a highly deteriorated pattern of metal mesh.

The distribution of metal wire exposure length is considered to be normal to facilitate further analysis. Indeed, it can be assumed that due to the errors in manual measurement of the length, the errors involved in grit-blasting processing and nozzle, the bin size, and lack of sufficient data in some cases lead to the deviation from normal behavior. Comparing the histograms in each group, it is obvious that by increasing the grit-blasting time the average metal wire exposure length increases as well. In the case of deviation from average, it is expected that increasing the time would lead to lower deviation as there is enough time to abrade the excessive polymer from the top of metal wires and achieve a more uniform profile. However, the comparison between the histograms shows no logical order. Therefore, the hypothesis is remained unanswered and requires further investigation.

Moreover, comparing groups 1-3, 4-6, and 7-9, separately, it can be deduced that increasing the stand-off distance highly affects the metal exposure length. It is due to the reduced velocity of sprayed grits at longer distances. Also, this parameter affects the effective radius of the grit-blasting zone on the sample, which will be further discussed in section 4.2.7.

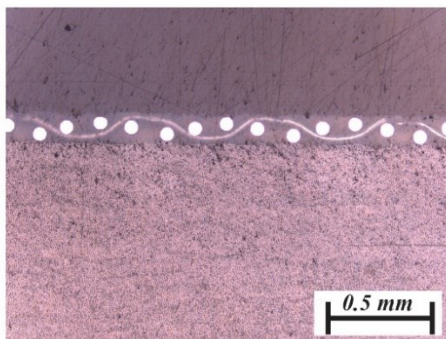
Last but not the least, the effect of pressure is obvious by comparing groups 1, 4, 7; 2, 5, 8; and 3, 6, 9. This way it is possible to examine the effect of grit-blasting pressure on the surface preparation state at constant time and stand-off distance. The most important finding of this comparison would be that pressure higher than 80 psi is highly risky since it can lead to failure of the surface preparation process and sample by damaging the metal wire mesh. It must be noticed that, and an over-blasted sample is failed, while an under-blasted sample can be further processed to obtain the desirable state.

The qualitative analysis in this section does not satisfy the requirements for an industrialized scenario. Hence, a quantitative analysis is carried out in section 4.2.4 explaining the effect of each parameter in detail.

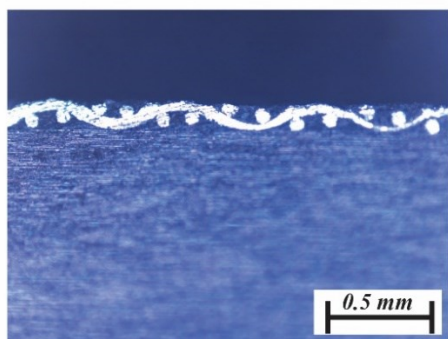
4.2.3. Validation through Optical Microscopy

In order to ascertain the observed state of surface preparation from the top of samples by the portable digital microscope, it is necessary to evaluate the cross-section of samples. The optical microscope images of some grit-blasted samples are provided in Figure 4.14 and Figure 4.15, along with the as-fabricated one revealing different states of surface preparation. As observable, the metal mesh is covered by resin in the under-blasted state, while in the case of proper-blasted, the resin is fully removed from the top of the metal mesh, exposing it without serious degradation. The slightly under-blasted state is comprised of mainly proper-blasted areas with marginal under-blasted areas. Further, analyzing slightly over-blasted samples, it can be indicated that not only the excessive resin is removed, but also the metal mesh pattern is damaged and/or the metal wire is abraded in some areas. Last, the over-blasted samples display either a high degree of damage in the metal mesh pattern or complete removal of the metal mesh as well as the excessive resin, which leads to exposure of the composite.

As-fabricated



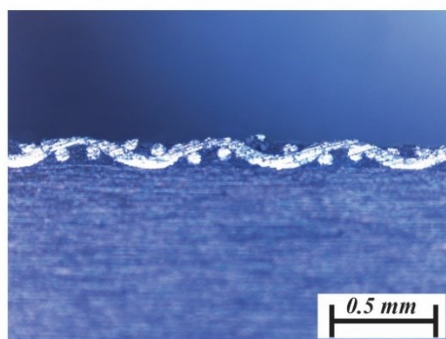
Sample 1, under-blasted



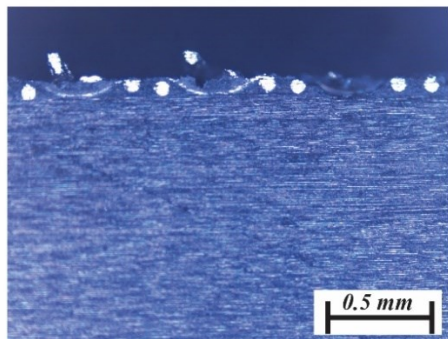
Sample 9, slightly under-blasted



Sample 11, properly-blasted



Sample 26, slightly over-blasted



Sample 23, over-blasted

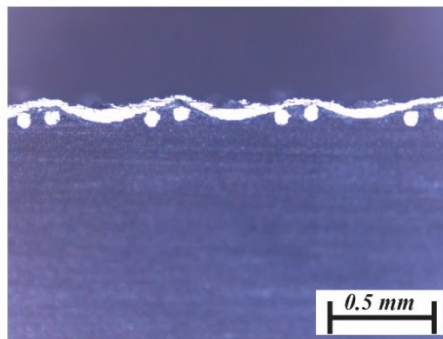


Figure 4.14. Low magnification optical microscope images of grit-blasted samples showing various states of surface preparation in comparison to as-fabricated state.

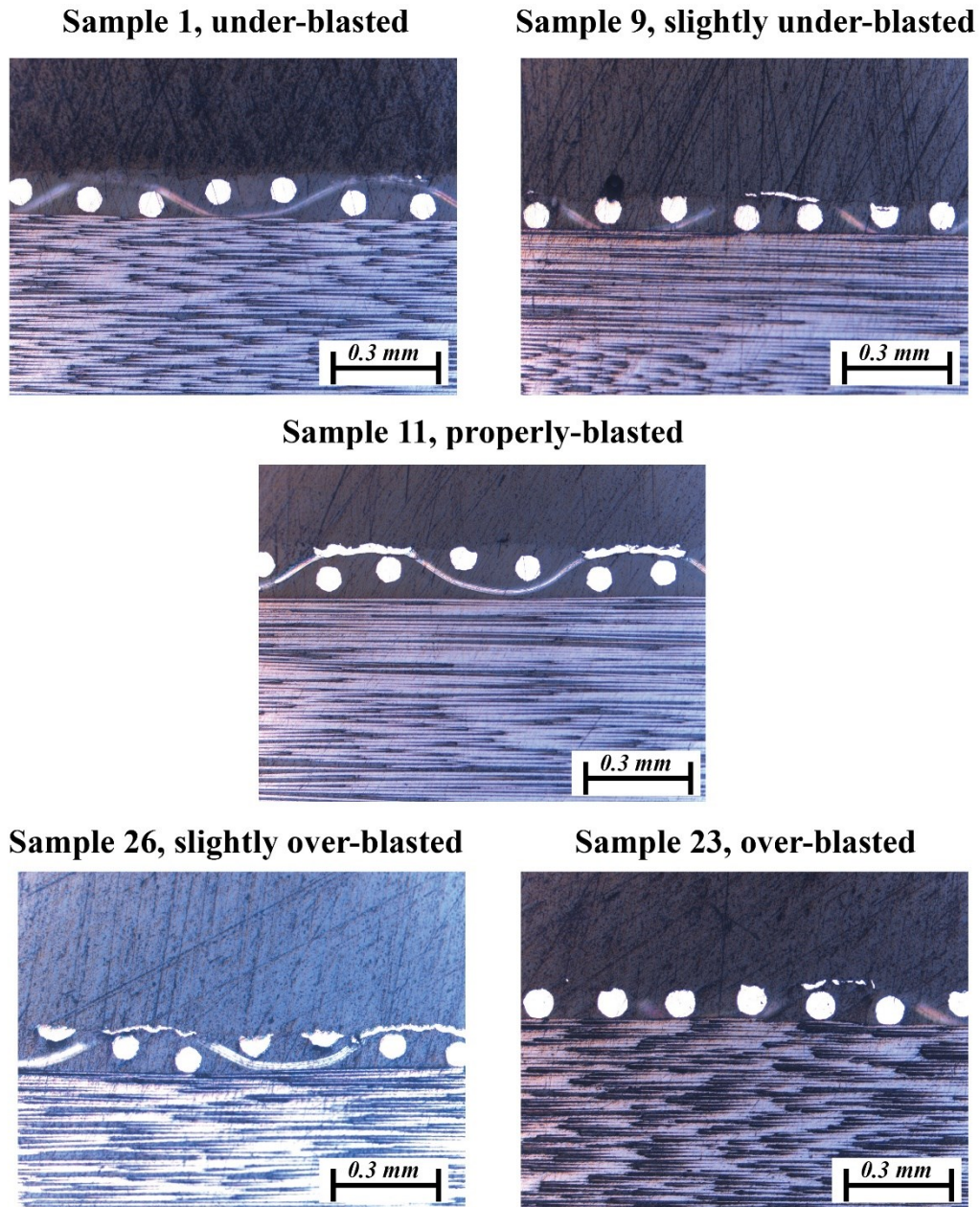


Figure 4.15. High magnification optical microscope images of grit-blasted samples showing various states of surface preparation in comparison to as-fabricated state.

In summary, the slightly under-blasted and proper-blasted states are the most favorable ones, as in the case of slightly over-blasted the final thermal spray coating process may inflict damage to the composite structure through the over-blasted areas, undermining the properties of the system. The

under-blasted samples are not considered as failed since they can be further processed with moderated blasting conditions to obtain the desirable state.

It is worthy to mention that optical microscopy is carried out without mounting the samples as the samples are required for further data acquisition to develop a computer vision inspection method detecting the surface preparation state of metal mesh/FRPC system.

4.2.4. Regression Analysis

As mentioned in section 4.2.2, it is not practical to extract x values for slightly over-blasted and over-blasted samples due to either degradation of the metal mesh pattern or complete abrasion of it. Hence, the regression models are developed with two sets of data. First, the over-blasted samples were disregarded, and the regression model fitted through interaction terms up to level two (Fit-1). Second, the mesh exposure level is estimated (Table 4.1 and Figure 4.16) based on the deterioration of metal mesh and composite, and with respect to the calculated mesh-exposure level of under-blasted and proper-blasted samples. Then, it was adhered to the set of data in the first case and an analogous regression model was fitted (Fit-2). Although the comparison of residuals distribution plotted in Figure 4.17 demonstrate that the former case is better fitted to the calculated results, it is incapable of predicting the corresponding mesh exposure of over-blasted samples. Hence, the third regression model is fitted by employing a box-cox transformation, which eventually provides both accuracies for predicted mesh exposure at all levels (Fit-3), and reasonable confidence intervals (CI). The corresponding mathematical model which is further subjected to optimization and generation of operational parameters maps can be presented as:

$$\ln M.E. (\%) = aP + bd + ct + g(Pd) + f(Pt) + M(dt)$$

the coefficients for the transformed response regression model are summarized in Table 4.2.

Table 4.1. The mesh exposure level, along with the results predicted by three different regression models and the confidence interval of the best fit based on the design of the experiment.

sample	P (psi)	d (cm)	t (sec)	x (μm)	h (μm)	Metal mesh exposure level (%)				
						Observed	Fit-1	Fit-2	Fit-3	95% CI (Fit-3)
1			60	142.3	89.5	24.6	24.8	36.6	19.2	(16.2, 22.6)
2		7	120	210.6	106.2	38.5	37.3	45.7	33.6	(28.3, 39.9)
3			180	267.4	115.5	46.3	49.8	54.9	59.0	(43.2, 80.4)
4			60	99.35	77.8	14.8	16.2	20.0	13.2	(10.8, 16.2)
5	60	10	120	166.7	95.9	30.0	28.4	28.8	24.1	(21.0, 27.7)
6			180	234.4	110.8	42.3	40.6	37.5	44.1	(35.5, 54.8)
7			60	53.9	66.9	5.7	7.7	3.5	9.1	(6.7, 12.3)
8		13	120	100.2	78.0	15.0	19.5	11.8	17.4	(14.2, 21.2)
9			180	196.4	103.2	36.0	31.3	20.1	33.0	(24.7, 44.1)
10			60	202.6	104.5	37.1	36.3	55.4	41.7	(33.9, 51.2)
11		7	120	300.6	118.5	48.8	48.2	72.8	61.7	(53.7, 70.9)
12			180	-	-	110*	60.0 ^R	90.3	91.3	(73.4, 113.6)
13			60	164.4	95.4	29.5	28.4	34.1	26.7	(23.2, 30.7)
14	80	10	120	255.9	114.1	45.1	39.9	51.1	41.2	(37.7, 45.0)
15			180	-	-	70*	51.4 ^R	68.1	63.5	(55.2, 73.1)
16			60	153.2	92.4	27.0	20.6	12.8	17.1	(13.8, 21.3)
17		13	120	162.2	94.8	29.0	31.7	29.4	27.5	(23.9, 31.7)
18			180	201.8	104.4	37.0	42.9	45.9	44.2	(35.5, 55.1)
19			60	-	-	100*	47.8 ^R	74.2	90.6	(67.5, 121.6)
20		7	120	-	-	120*	59.0 ^R	99.9	113.2	(92.9, 138.0)
21			180	-	-	130*	70.2 ^R	125.6	141.4	(105.4, 189.8)
22			60	194	102.6	35.5	40.6	48.1	54.0	(43.7, 66.8)
23	100	10	120	-	-	65*	51.5 ^R	73.4	70.3	(61.1, 80.8)
24			180	-	-	95*	62.3 ^R	98.7	91.5	(73.4, 114.0)
25			60	172.5	97.4	31.2	33.4	22.1	32.2	(23.6, 43.9)
26		13	120	293.8	118.1	48.4	43.9	46.9	43.7	(35.3, 54.0)
27			180	-	-	60*	54.4	71.8	59.2	(45.6, 76.9)

* denotes the value is an estimation

R denotes the predicted values is excessively different from the real one

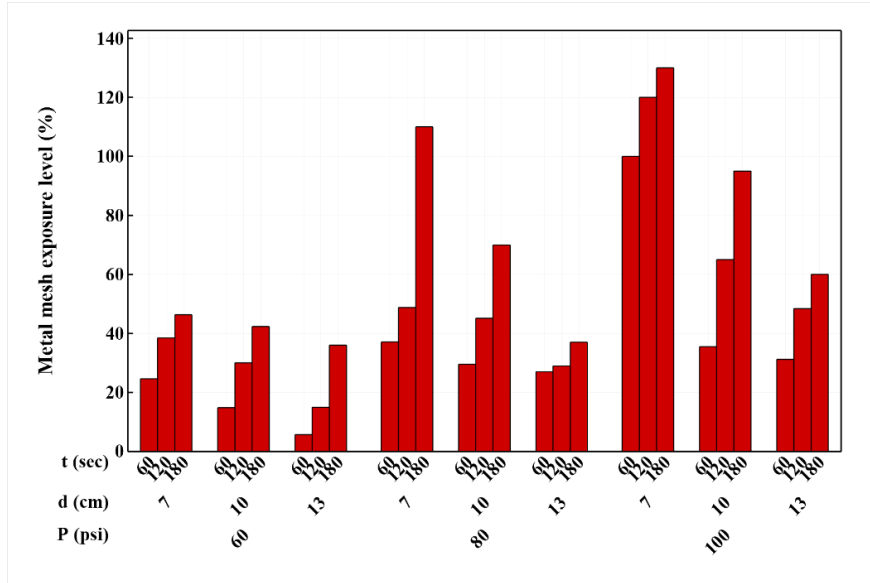


Figure 4.16. Bar plot of mesh exposure level versus grit-blasting parameters (observed and estimated data).

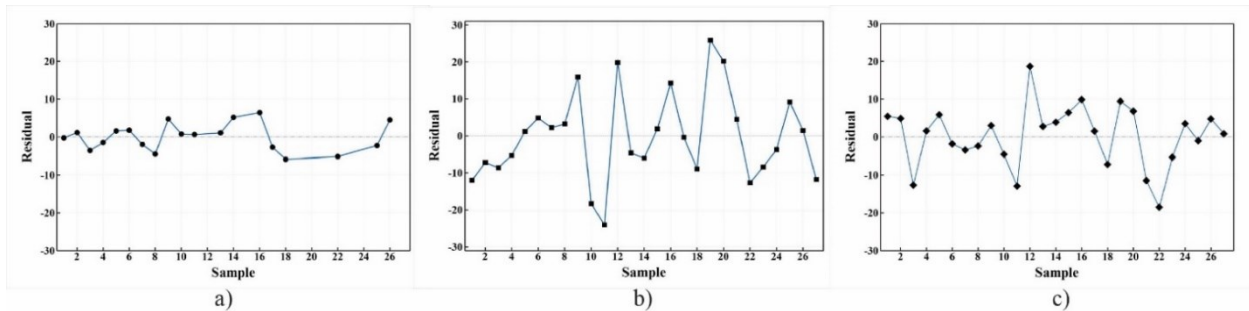


Figure 4.17. Plot of residuals for predicted values of mesh exposure level using a) Fit-1, b) Fit-2, and c) Fit-3, from observed/estimated ones.

Table 4.2. Coefficients for transformed response regression model (Fit-3).

Term	Coefficient	Value	P-Value
P (psi)	<i>a</i>	0.05584	0.000
d (cm)	<i>b</i>	-0.0642	0.203
t (sec)	<i>c</i>	0.01628	0.002
P (psi)*d (cm)	<i>g</i>	-0.001216	0.095
P (psi)*t (sec)	<i>f</i>	-0.000141	0.007
d (cm)*t (sec)	<i>m</i>	0.000226	0.501

4.2.5. Operation Window Map

Considering the number of variables in the developed regression model, it is impractical to generate fully comprehensible graphs for evaluating the behavior of mesh exposure level versus variables. Therefore, two-dimensional operation maps are generated depicting the mesh exposure level versus P and t , at various d based on the regression model. The developed maps are provided for five various d , that is 13, 11, 10, 9, and 7 cm, for the p and t in the range of 60-100 psi and 60-180 sec, respectively (Figure 4.18-Figure 4.22).

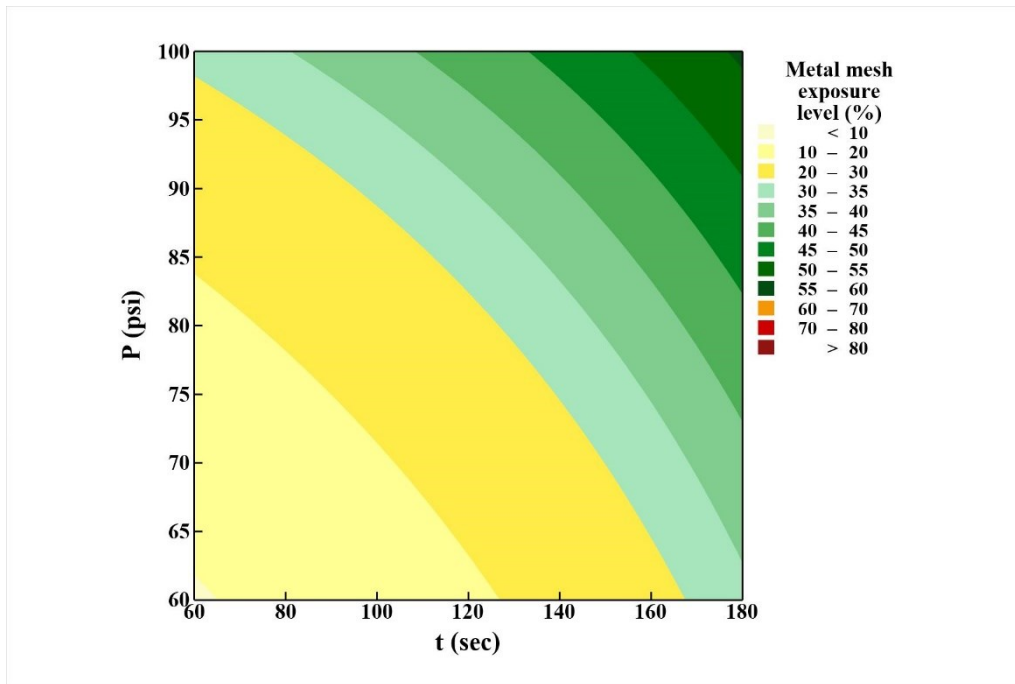


Figure 4.18. 2D surface map of mesh exposure level dependent on P and t , at $d = 13$ cm.

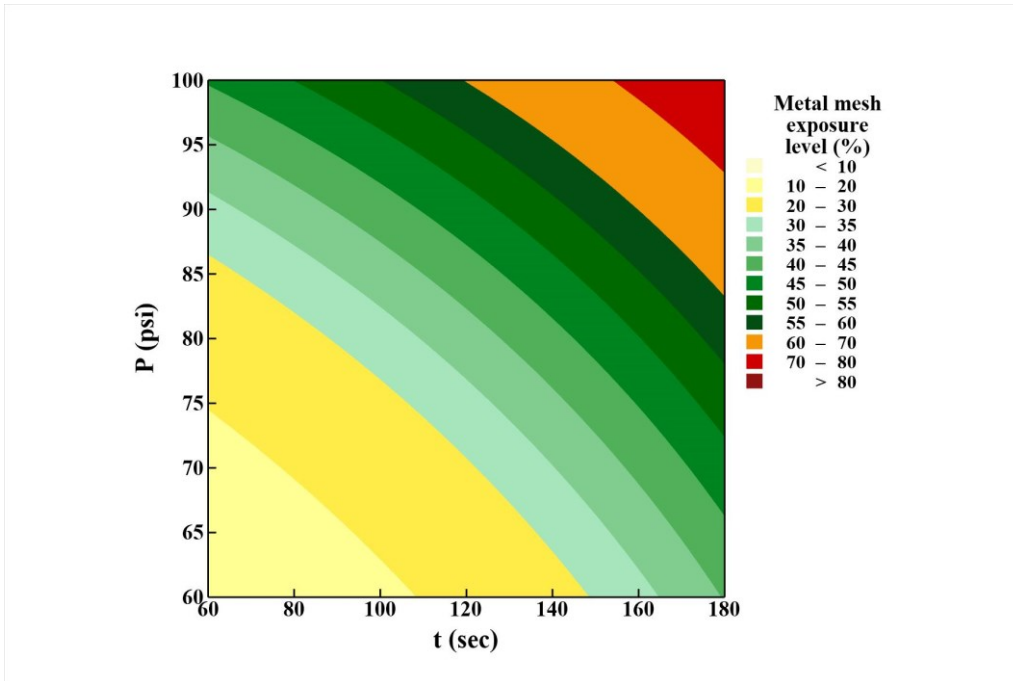


Figure 4.19. 2D surface map of mesh exposure level dependent on P and t , at $d = 11$ cm.

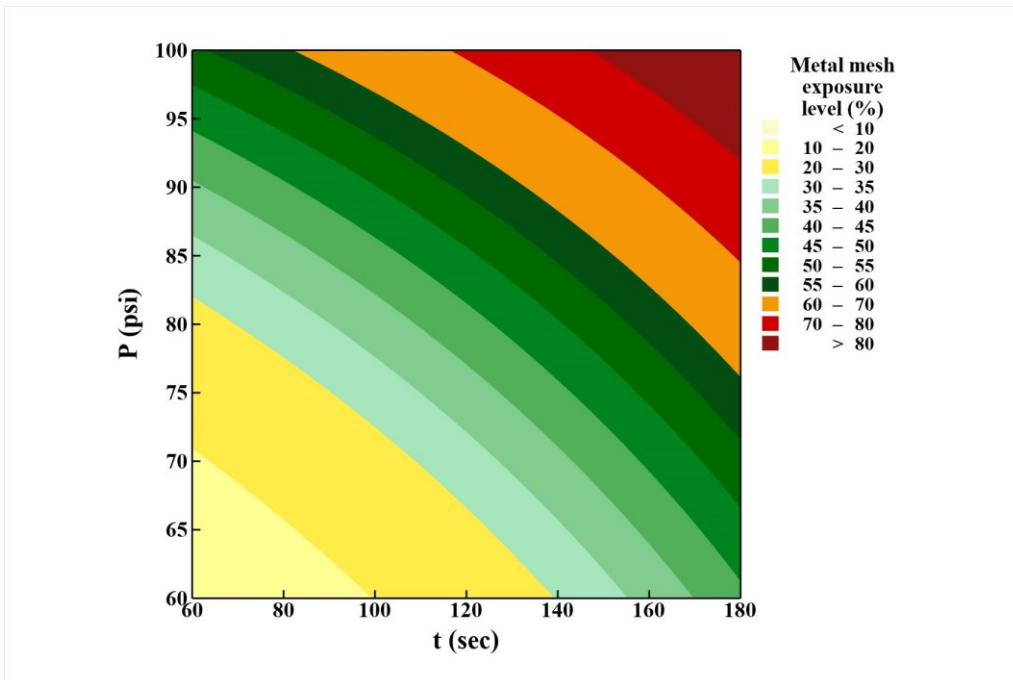


Figure 4.20. 2D surface map of mesh exposure level dependent on P and t , at $d = 10$ cm.

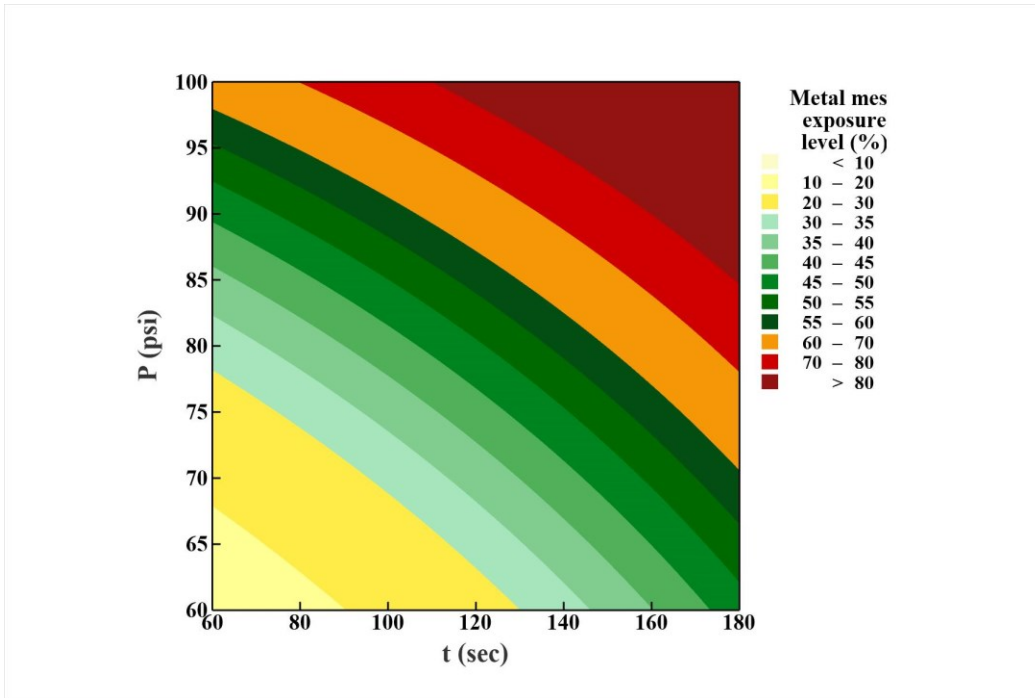


Figure 4.21. 2D surface map of mesh exposure level dependent on P and t , at $d = 9$ cm.

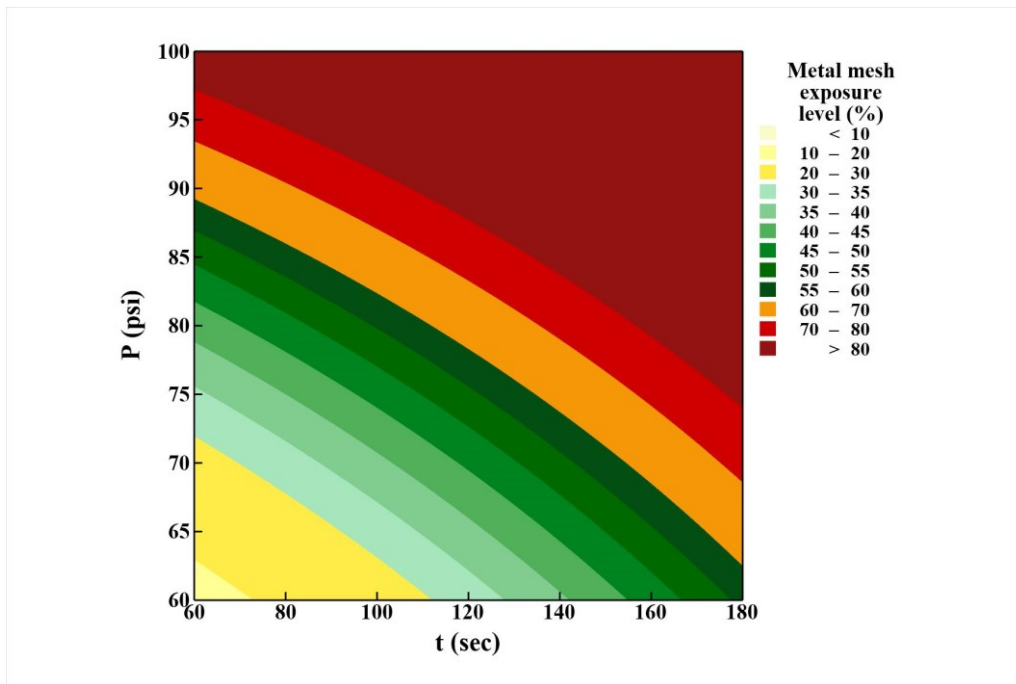


Figure 4.22. 2D surface map of mesh exposure level dependent on P and t , at $d = 7$ cm.

As observable, increasing d from 7 to 11 cm widens the safe window (30-60% mesh exposure) for grit-blasting with moderate P and t (i.e., 70-80 psi for a duration of 90-150 sec). Whereas, further increasing d requires higher P and t for obtaining proper mesh exposure levels. Hence, it can be expected that the set of parameters in the range of $P = 75-85$ psi, $d = 10-11$ cm, and $t = 90-120$ sec, not only provide a desirable mesh exposure level (35-55%) but also avoid damage to the mesh and composite with a good degree of safety. This is vitally important since an under-blasted part can be further grit-blasted to obtain the proper surface preparation state, in contrast to an over-blasted part.

4.2.6. Optimization of Parameters

In addition to the operation parameter maps, the regression model is subjected to an optimization targeting 47.5 % mesh exposure, in the P and t ranges of 60-85 psi and 60-150 sec. This step is carried out to minimize the grit-blasting time and reduce the probability of failure in the surface preparation process. The former is especially important in an industrial application since the grit-blasting time not only directly affects the production rate, but also can incur excessive usage and cost of the grit material. Optimization parameters and solutions are summarized in Table 4.3

Table 4.3. Optimization parameters and solutions for enhancing safe windows and reducing operation time.

Response	Goal	Lower	Target	Upper	Weight	Importance
Metal mesh exposure level (%)	Target	35	47.5	60	0.1	5

Solutions	P (psi)	d (cm)	t (sec)	Metal mesh exposure level (%) – Fit3
1	77	10	146	47.4617
2	64	7	150	48.9160
3	85	11	131	45.7097
4	62	7	150	45.6536
5	77	7	85	45.5630
6	85	8	60	45.5453

With respect to the fact that d has no direct influence on the economical side of the process, P and t can be analyzed more in detail. Indeed, one of the two parameters should be set as the most influential criteria. In the scenario, where the feed rate of the grit material is not affected by the pressure, one can disregard P and select parameter sets based on the optimum t . Considering this to be true, solutions 5 and 6 in Table 4.3 are the most effective parameters leading to a favorable surface preparation state, avoiding damage to the system, and reflecting economic benefits.

4.2.7. Effective Radius of the Gun

The t parameter analyzed in this study is only valid for the case of studied coupons. However, in a real situation, the time of grit-blasting must be evaluated and optimized by means of the effective radius of the gun and gun movement speed. The grit-blasting parameters such as P and d pose an effect on the effective grit-blasting zone, along with the nozzle diameter. Therefore, it is necessary to investigate the effect of these parameters on effective radius and formulate it, in order to find the effective grit-blasting time.

In this regard, six additional grit-blasting tests are carried out on metal mesh/CFRPs, where the sample is kept constant allowing grit-blasting of a certain area. This set of tests is carried out for a long grit-blasting time (120 sec) where the composite is completely eroded in the effective grit-blasting zone (Figure 4.23). P and d are selected based on the initial design of the experiment in this study, that is 80, and 100 psi; 7, 10, and 13 cm, respectively. As it can be observed, the grit-blasting area can be divided into four regions 1- the primary (R_p), 2- secondary (R_s), 3- transition, and 4- light effect. Considering the long processing time, it can be assumed the effect of transition and light effect areas can be disregarded in the case of optimizing the time for moving samples. The extracted radii from the 6 tests are summarized in Table 4.4.

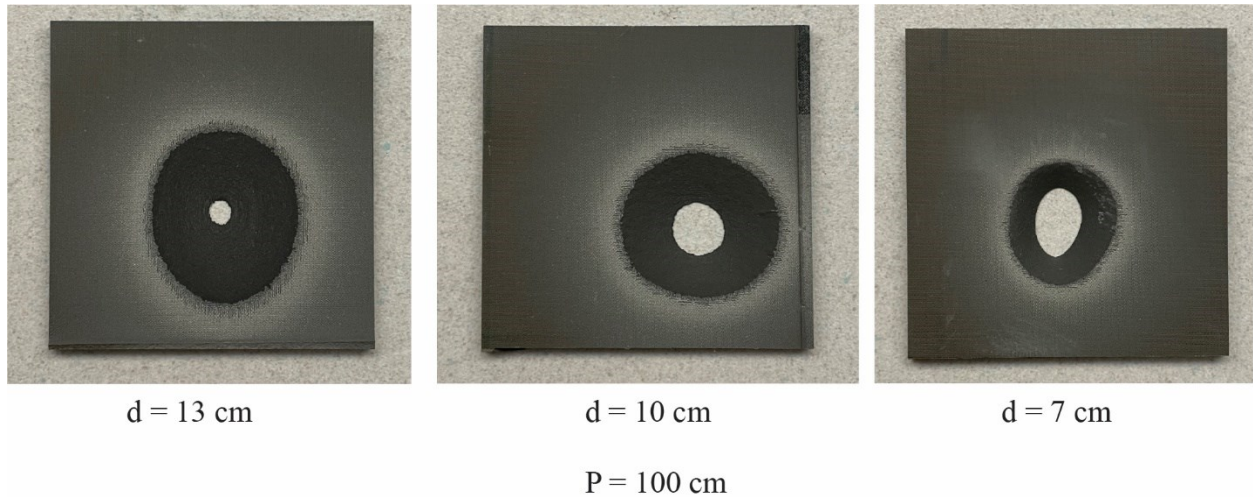


Figure 4.23. Image of a sample grit-blasted at one point under the pressure of 100 psi at various distances demonstrating the four regions of the grit-blasting zone.

Table 4.4. The effective radius of grit-blasting at various pressure and distances.

P (psi)	d (cm)	R_p (mm)	R_s (mm)
100	7	4.8	9.6
100	10	3.3	11.0
100	13	1.8	12.9
80	7	4.4	9.4
80	10	3.0	10.0
80	13	1.5	12.0

Employing the data and considering its behavior to be linear, the effective radius of grit-blasting in primary and secondary regions can be estimated as:

$$R_p = 0.052 P - 0.126 d$$

$$R_s = 0.458 P + 0.707 d$$

A noticeable phenomenon is the reduction of R_p and surge of R_s with increasing the d , which is due to effect d on erodent of sprayed grits. Employing the effective radius and having the speed of grit-blasting (in this case 5 mm/s), it is possible to calculate the effective grit-blasting time.

4.2.8. Surface Roughness

The surface roughness of the samples measured by a profilometer over a 4 mm profile is reported in Table 4.5.

Table 4.5. Measured surface roughness of the grit-blasted samples.

sample	Ra (μm)
1	3.740
2	4.785
3	5.248
4	3.703
5	4.605
6	5.157
7	2.579
8	3.115
9	4.149
10	5.351
11	6.645
12	-
13	4.124
14	6.051
15	6.956
16	2.891
17	3.260
18	4.188
19	-
20	-
21	-
22	3.475
23	7.068
24	-
25	3.990
26	4.969
27	6.643

Comparing the surface roughness values, it can be deduced that increasing P and t leads to higher surface roughness while increasing d results in lower surface roughness. Considering that surface roughness is an important parameter influencing the formation of coating and its properties, it requires further experimentation to find the optimized value. On the other hand, the acquired surface roughness for samples 3, 11, 14, and 26 are all high enough for providing a mechanical

anchor in the coating process. Indeed, the above-mentioned samples present both the criteria of proper mesh exposure level and roughness. From the viewpoint of economic efficiency, samples 11 and 14 are the most suitable ones as a result of lower processing time, while avoiding damage to the mesh and composite structure.

4.2.9. Effect of Grits

Another influential factor in the efficiency of the grit-blasting process is the shape of grit materials. This topic requires comprehensive examination, however, herein the unused and used grits are analyzed by optical microscope to detect the shape change of the materials during the surface preparation process. As is observable in Figure 4.24, the sharp-edged grits undergo deformation after some processing time. The used grits with a less sharp-edged shape present a lower erosion effect and can lead to deviation of results. Moreover, the inclusions and impurities are detectable in the used grits, which denotes the need for cleaning the cabinet prior to processing. Hence, it is vital to check the grits and renew them after several processing times to assure consistency in the results, especially in industrial cases.



Figure 4.24. Digital microscope images of the unused and used grits.

Chapter 5: Conclusion and Future Work

5.1. Conclusion

In this study, the grit-blasting process as the primary surface preparation method of metal mesh incorporated FRPCs for thermal spray coating is quantitatively analyzed. The most exquisite purpose of this investigation is to optimize the main grit-blasting parameters and develop operational maps for the estimation of the surface preparation state of the composite prior to the coating process. Moreover, the acquired data will be further utilized to develop a versatile computer vision inspection method for in-situ analysis.

In order to overcome the in-service limitations of FRPCs, surface coating is a potential resolution. However, the coating process of FRPCs, especially by thermal spray methods, is challenging itself due to the low melting temperature of the polymeric-based substrate and the vulnerability of fibers to the impact of impinging particles. To prevent failure of the composite during the thermal spraying process, a superficially incorporated metal wire mesh in the composite proved to be an effective way to dissipate the heat and act as a bond coat. Nevertheless, surface preparation, such as grit-blasting, is required to expose the metal mesh covered by polymer during the manufacturing step.

In the present research, metal mesh incorporated CFRP plates are fabricated employing hand lay-up of prepregs and autoclave curing. Thereafter, two surface preparation methods, that is sandpaper polishing and grit-blasting, are tested. The latter approach is studied more comprehensively employing a homemade automated setup to investigate the effect of various parameters on the surface preparation state and develop a quantitative measure for future references. In this regard, three primary grit-blasting parameters of pressure, distance, and time are examined at three different levels throughout the design of the experiment. For the sake of characterization, an affordable, portable digital microscope is used to provide high magnification

images from the top-view of exposed mesh. Moreover, the results are validated through optical microscopy of the cross-section of the samples.

In the case of sandpaper polishing, the results prove that this method is not an appropriate alternative to grit-blasting since during the process both excessive resin and metal wires are polished simultaneously resulting in a polished surface with low surface roughness.

For the case of grit-blasting, A correlation is found between the exposure length of wires observed from the top-view and the exposure level of metal mesh. Therefore, a regression model is developed on this basis estimating the exposure level as a function of pressure, distance, and time in the ranges of 60-100 psi, 7-13 cm, and 60-180 sec. Employing the regression model, operation window maps are generated clarifying the estimated mesh exposure level versus pressure and time, at various distances. Besides, Considering the economics of the process, the parameters are optimized revealing a parameter set of 85 psi, 8 cm, and 60 sec to be the appropriate condition for achieving a proper mesh exposure level of 45%.

Analyzing the effective radius of grit-blasting, it can be indicated that the two main regions of the grit-blasting zone are dependent on the nozzle radius, pressure, and distance. Having the relations for the radius of these two regions, one can calculate the effective grit-blasting time of each area and further control the grit-blasting speed to obtain a consistent surface preparation state all over a bulky component.

Another crucial feature inspected in this work is the effect of grit-blasting parameters on the surface roughness of samples. The results prove that increasing pressure and time lead to higher surface roughness on contrary to the distance. Therefore, the parameters should be selected in a

manner to achieve a proper surface roughness, while obtaining a proper mesh exposure level and preventing damage to metal mesh and composite.

Last but not the least, the shape of grits is explored before and after the experimentation, elucidating the importance of checking the quality and shape of the grits on the process efficiency. Indeed, the rounded grits are weaker in terms of eroding the excessive resin, which can lead to longer processing time and higher cost.

5.2. Future Work

The present research study has contributed to the surface preparation of metal mesh/FRPCs for thermal spray coating. However, further research is required to develop the grit-blasting process and the inspection procedure for an industrial application. Further investigations in this field can be extended to:

- Investigating the effect of application of adhesive film before metal mesh on the FRPC lay-up to prevent uncovered mesh during manufacturing of the substrate.
- Investigating the effect of vacuum gauge distance from the sample on the wetting of the metal mesh by resin during manufacturing.
- Exploring softer and finer grit materials provides higher accuracy in removing the resin while maintaining the metal wires.
- Examining alternative surface preparation methods such as chemical treatment for exposing the metal mesh prior to the coating step.

- Deposition of surface coating on the sample prepared with a similar condition to further validate the importance of an optimized surface preparation state.
- Developing a computer vision inspection method for in-situ characterization of the surface preparation method with the capability to decide the next step of the process and regulate the grit-blasting parameters.

References

- [1] B.T. Åström, Manufacturing of Polymer Composites, Manufacturing of Polymer Composites. (2018).
- [2] S. Erden, K. Ho, Fiber reinforced composites, Fiber Technology for Fiber-Reinforced Composites. (2017) 51–79.
- [3] P.K. Mallick, Fiber-Reinforced Composites: Materials, Manufacturing, and Design, Third Edition, (2007).
- [4] L.C. Hollaway, A review of the present and future utilization of FRP composites in the civil infrastructure with reference to their important in-service properties, Construction and Building Materials. 24 (2010) 2419–2445.
- [5] T.F.A. Santos, G.C. Vasconcelos, W.A. de Souza, M.L. Costa, E.C. Botelho, Suitability of carbon fiber-reinforced polymers as power cable cores: Galvanic corrosion and thermal stability evaluation, Materials & Design. 65 (2015) 780–788.
- [6] F.-L. Jin, S.-Y. Lee, S.-J. Park, A. Info, Polymer matrices for carbon fiber-reinforced polymer composites, Carbon Letters. 14 (2013) 76–88.
- [7] S. Kalpakjian, S.S.- agenda, 2014, Manufacturing processes for engineering materials–5th edition.
- [8] P. Pichler, B.J. Simonds, J.W. Sowards, G. Pottlacher, Measurements of thermophysical properties of solid and liquid NIST SRM 316L stainless steel, Journal of Materials Science. 55 (2020) 4081–4093.
- [9] I. Tolosa, F. Garcíandía, F. Zubiri, F. Zapirain, A. Esnaola, Study of mechanical properties of AISI 316 stainless steel processed by “selective laser melting”, following different manufacturing strategies, The International Journal of Advanced Manufacturing Technology 2010 51:5. 51 (2010) 639–647.
- [10] K.E. Gilcrist, S.D. Preston, The Thermal Diffusivity/Conductivity of 316 Stainless Steel Powders in Air and Nitric Acid Mixtures at Room Temperature, Thermal Conductivity 18. (1985) 713–722.
- [11] N. den Uijl, Resistance spot welding of advanced high strength steels, (2015).
- [12] J. Schmitt, T.I.-C.R. Physique, 2018, New developments of advanced high-strength steels for automotive applications, Elsevier.
- [13] J. Davis, Aluminum and aluminum alloys, 1993.
- [14] J. Davis, Copper and copper alloys, 2001.
- [15] G.J. London, Titanium Matrix Composites, 3 (2007) 367–382.
- [16] P. Auerkari, Mechanical and physical properties of engineering alumina ceramics, 1996.

- [17] D.J. Green, *An Introduction to the Mechanical Properties of Ceramics*, An Introduction to the Mechanical Properties of Ceramics. (1998).
- [18] H. Abderrazak, E.H.-P. and applications of Silicon, 2011, *Silicon carbide: synthesis and properties*, Books.Google.Com.
- [19] D. Green, J. Winandy, D.K.-U.F. Service, undefined Forest, 1999, *Mechanical properties of wood*, Fs.Usda.Gov.
- [20] B.M. Suleiman, J. Larfeldt, B. Leckner, M. Gustavsson, *Thermal conductivity and diffusivity of wood*, *Wood Science and Technology*. 33 (1999) 465–473.
- [21] *Properties evaluation of fiber reinforced polymers and their constituent materials used in structures—A review*, Elsevier.
- [22] I.A.-J. of M.R. and Technology, 2019, *Investigation the conductivity of carbon fiber composites focusing on measurement techniques under dynamic and static loads*, Elsevier.
- [23] X. Luo, D.C.-C.P.B. Engineering, 1999, *Electromagnetic interference shielding using continuous carbon-fiber carbon-matrix and polymer-matrix composites*, Elsevier.
- [24] H. Mahmood, S. Unterberger, A.P.C. Science, 2017, *Tuning electrical and thermal properties in epoxy/glass composites by graphene-based interphase*, Mdpi.Com.
- [25] S. Wang, J.Q.-C.P.B. Engineering, undefined 2010, *Enhancing thermal conductivity of glass fiber/polymer composites through carbon nanotubes incorporation*, Elsevier.
- [26] D. Rajak, D. Pagar, P. Menezes, E.L.- Polymers, 2019, *Fiber-reinforced polymer composites: Manufacturing, properties, and applications*.
- [27] A.G. Gibson, P.N.H. Wright, Y.-S. Wu, A.P. Mouritz, Z. Mathys, C.P. Gardiner, *The integrity of polymer composites during and after fire*, *Journals.Sagepub.Com*. 38 (2004) 1283–1307.
- [28] A. Mouritz, S. Feih, E. Kandare, 2009, *Review of fire structural modelling of polymer composites*, Elsevier.
- [29] B. Alemour, O. Badran, M.H.-J. of A. Technology, 2019, *A review of using conductive composite materials in solving lightning strike and ice accumulation problems in aviation*, SciELO Brasil.
- [30] J. Hu, Y. Huang, Y. Yao, G. Pan, J. Sun, X. Zeng, R. Sun, J. bin Xu, B. Song, C.P. Wong, *Polymer Composite with Improved Thermal Conductivity by Constructing a Hierarchically Ordered Three-Dimensional Interconnected Network of BN*, *ACS Applied Materials and Interfaces*. 9 (2017) 13544–13553.
- [31] A. Ballo, T.N.-B. of D. Biomaterials, undefined 2017, *Biocompatibility of fiber-reinforced composites for dental applications*, Elsevier.
- [32] R.P.- Fibers, undefined 2016, *Carbon fiber biocompatibility for implants*.

- [33] L. Guadagno, L. Vertuccio, C. Naddeo, M.R.- *Polymers*, 2019, Electrical current map and bulk conductivity of carbon fiber-reinforced nanocomposites.
- [34] A. Haghbin, G. Liaghat, H. Hadavinia, A. Arabi, M.P.- *Materials*, 2017, Enhancement of the electrical conductivity and interlaminar shear strength of CNT/GFRP hierarchical composite using an electrophoretic deposition technique.
- [35] K. Hamdi, Z. Aboura, W. Harizi, K. Khellil, Improvement of the electrical conductivity of carbon fiber reinforced polymer by incorporation of nanofillers and the resulting thermal and mechanical behavior, *Journal of Composite Materials*. 52 (2018) 1495–1503.
- [36] A. Adeniyi, O. Agboola, E. Sadiku, 2016, *Thermoplastic-thermoset nanostructured polymer blends*, Elsevier.
- [37] A.K. Ghosh, M. Dwivedi, Processability in Open Mould Processing of Polymeric Composites, *Processability of Polymeric Composites*. (2020) 179–203.
- [38] H. Che, M. Gagné, P.S.M. Rajesh, J.E. Klemberg-Sapieha, F. Sirois, D. Therriault, S. Yue, Metallization of Carbon Fiber Reinforced Polymers for Lightning Strike Protection, *Journal of Materials Engineering and Performance*. 27 (2018) 5205–5211.
- [39] R. Li, W. Xu, D. Zhang, R.; Li, W.; Xu, D. Zhang, impacts of thermal and mechanical cycles on electro-thermal anti-icing system of CFRP laminates embedding sprayable metal film.
- [40] C. Karch, C.M.-2016 33rd I.C. 2016, Lightning protection of carbon fibre reinforced plastics—An overview, *Ieeexplore*.
- [41] A.S. Chen, D.P. Almond, B. Harris, Impact damage growth in composites under fatigue conditions monitored by acoustography, *International Journal of Fatigue*. 24 (2002) 257–261. [https://doi.org/10.1016/S0142-1123\(01\)00080-9](https://doi.org/10.1016/S0142-1123(01)00080-9).
- [42] P. Tran, Q.T. Nguyen, K.T. Lau, Fire performance of polymer-based composites for maritime infrastructure, *Composites Part B: Engineering*. 155 (2018) 31–48.
- [43] A.S. Verma, S.G.P. Castro, Z. Jiang, J.J.E. Teuwen, Numerical investigation of rain droplet impact on offshore wind turbine blades under different rainfall conditions: A parametric study, *Composite Structures*. 241 (2020) 112096.
- [44] J. Sun, S. Zhou, K. Yamanaka, H. Bina, Y. Ichikawa, H. Saito, K. Ogawa, A. Chiba, Adhesion mechanism of temperature effects on Sn coating on the carbon fiber reinforced polymer substrate by cold spray, *Arxiv.Org*.
- [45] H. Che, X. Chu, P. Vo, S. Yue, Metallization of Various Polymers by Cold Spray, *Journal of Thermal Spray Technology*. 27 (2018) 169–178.
- [46] R. Gonzalez, H. Ashrafizadeh, A. Lopera, P. Mertiny, A. McDonald, A Review of Thermal Spray Metallization of Polymer-Based Structures, *Journal of Thermal Spray Technology*. 25 (2016) 897–919

- [47] S. Yan, X. Zhou, H. Zhang, S. Dong, X. Li, J. Jiang, X. Cao, HVOF-Sprayed AlSi50 Alloy Coatings as a Novel Electrothermal Anti-icing/De-icing System for Polymer-based Composite Structures, *Journal of Thermal Spray Technology*. 30 (2021) 2161–2173.
- [48] P. Fallah, S. Rajagopalan, A. McDonald, S.Y.-S. and Coatings, undefined 2020, Development of hybrid metallic coatings on carbon fiber-reinforced polymers (CFRPs) by cold spray deposition of copper-assisted copper electroplating, Elsevier.
- [49] A. Lopera-Valle, A. McDonald, Application of Flame-Sprayed Coatings as Heating Elements for Polymer-Based Composite Structures, *Journal of Thermal Spray Technology*. 24 (2015) 1289–1301.
- [50] V. Bortolussi, B. Figliuzzi, F. Willot, M. Faessel, M. Jeandin, Electrical Conductivity of Metal–Polymer Cold Spray Composite Coatings onto Carbon Fiber-Reinforced Polymer, *Journal of Thermal Spray Technology*. 29 (2020) 642–656.
- [51] A. Rahimi, M.H.-J. 2021, Thermal Spray Coating on Polymeric Composite for De-Icing and Anti-Icing Applications, ASME digital collection.
- [52] S.E.-H. of A. and S. Preparation, 2011, Material surface preparation techniques, Elsevier.
- [53] S.E.-H. of A. and S. Preparation, 2011, Surface preparation of thermoplastics, thermosets, and elastomers, Elsevier.
- [54] S. Hoa, Principles of the manufacturing of composite materials, 2009.
- [55] T. Sathishkumar, S.S.-J. of reinforced, undefined 2014, Glass fiber-reinforced polymer composites—a review, *Journals.Sagepub.Com*. 33 (2014) 1258–1275.
- [56] D. Cousins, Y. Suzuki, R. Murray, J.S, 2019, Recycling glass fiber thermoplastic composites from wind turbine blades, Elsevier.
- [57] V. Alzamora Guzman, P. Brøndsted, Effects of moisture on glass fiber-reinforced polymer composites, *Journal of Composite Materials*. 49 (2015) 911–920.
- [58] T.K. Das, P. Ghosh, N.C. Das, Preparation, development, outcomes, and application versatility of carbon fiber-based polymer composites: a review, *Advanced Composites and Hybrid Materials*. 2 (2019) 214–233.
- [59] Y. Liu, S.K.-P. Reviews, 2012, Recent progress in fabrication, structure, and properties of carbon fibers, *Taylor & Francis*. 52 (2012) 234–258.
- [60] E. Frank, L.M. Steudle, D. Ingildeev, J.M. Spçrl, M.R. Buchmeiser, M.R. Buchmeiser, Carbon fibers: precursor systems, processing, structure, and properties, *Wiley Online Library*. 53 (2014) 5262–5298.
- [61] G. Yang, M. Park, S.P.-C. Communications, 2019, Recent progresses of fabrication and characterization of fibers-reinforced composites: A review, Elsevier.

- [62] K. Pang, R. Kotek, A.T.-P. in polymer science, 2006, Review of conventional and novel polymerization processes for polyesters, Elsevier.
- [63] D.C.-M.S. and E.R. Reports, 2017, Processing-structure-property relationships of continuous carbon fiber polymer-matrix composites, Elsevier.
- [64] M.M.-F. reinforced polymers-the technology applied for, 2013, Introduction of fiber-reinforced polymers– polymers and composites: concepts, properties and processes, Intechopen.Com.
- [65] G. Bass, M. Becker, D. Heath, S.C.-B. Science, 2020, Polymers: Basic Principles, Elsevier.
- [66] L. McKeen, Fatigue and tribological properties of plastics and elastomers, 2016.
- [67] N. Paluvai, S. Mohanty, S.N.-P.-P. Technology, 2014, Synthesis and modifications of epoxy resins and their composites: a review, Taylor & Francis. 53 (2014) 1723–1758.
- [68] A. Toldy, B. Szolnoki, G.M.-P. degradation and stability, 2011, Flame retardancy of fiber-reinforced epoxy resin composites for aerospace applications, Elsevier.
- [69] E. Petrie, Handbook of adhesives and sealants, 2007.
- [70] D. Shah, K. Patel, S. Joshi, B. Modi, A.P.-T., 2019, Thermo-mechanical characterization of carbon fiber composites with different epoxy resin systems, Elsevier.
- [71] W. Gao, X. Cao, M. Chen, K. Chen, S.L.P. Science, 2021, Tertiary-amine-terminated polybutadiene and butadiene acrylonitrile: Synthesis and application in the modification of epoxy resins, Wiley Online Library. 138 (2020).
- [72] J. Fink, Reactive polymers: fundamentals and applications: a concise guide to industrial polymers, 2017.
- [73] J. Scheirs, T. Long, Modern polyesters: chemistry and technology of polyesters and copolyesters, 2005.
- [74] H. Saleh, Polyester, 2012.
- [75] A. Kandelbauer, G. Tondi, O.Z.-H. of thermoset, 2022, Unsaturated polyesters and vinyl esters, Elsevier.
- [76] R. Deepak, J. Johnson, V. Arumugaprabu, Tae, J. Ko, Mechanical property, wear characteristics, machining and moisture absorption studies on vinyl ester composites—a review, Springer. 11 (2019) 2455–2470.
- [77] A. Mouritz, Introduction to aerospace materials, 2012.
- [78] R. Iredale, C. Ward, I.H.-P. in P. Science, 2017, Modern advances in bismaleimide resin technology: A 21st century perspective on the chemistry of addition polyimides, Elsevier.
- [79] M. Biron, Thermoplastics and thermoplastic composites, 2018.

- [80] O. Olabisi, K. Adewale, Handbook of thermoplastics, 2016.
- [81] B. Liu, A. Xu, L. Bao, Preparation of carbon fiber-reinforced thermoplastics with high fiber volume fraction and high heat-resistant properties, *Journal of Thermoplastic Composite Materials*. 30 (2017) 724–737.
- [82] Yang X, Zhao J, Wu K, Yang M, Wu J, Zhang X, Zhang X, Li Q. Making a strong adhesion between polyetherketoneketone and carbon nanotube fiber through an electro strategy. *Composites Science and Technology*. 2019 Jun 16;177:81-7.
- [83] M.D.-H. of environmental degradation of materials, undefined 2018, Thermal spray coatings, Elsevier.
- [84] Amin S, Panchal H. A review on thermal spray coating processes. *International Journal of Current Trends in Engineering & Research*. 2016 Apr 4;2(4):556-63.
- [85] P.V.-C. materials processing, 1st edition, undefined 2014, Thermal spray coating processes, Researchportal.Tuni.Fi.
- [86] N. Espallargas, Future development of thermal spray coatings: Types, designs, manufacture and applications, 2015.
- [87] I.C. Roata, C. Croitoru, A. Pascu, E.M. Stanciu, Photocatalytic coatings via thermal spraying: A mini review, *AIMS Materials Science*. 6 (2019) 335–353.
- [88] R. Gonzalez, A. McDonald, P. Mertiny, Effect of flame-sprayed Al–12Si coatings on the failure behaviour of pressurized fibre-reinforced composite tubes, *Polymer Testing*. 32 (2013) 1522–1528.
- [89] A. Lopera-Valle, A. McDonald, Flame-sprayed coatings as de-icing elements for fiber-reinforced polymer composite structures: Modeling and experimentation, *International Journal of Heat and Mass Transfer*. 97 (2016) 56–65.
- [90] L. Fang, J. Huang, Y. Liu, B. Zhang, H.L.-S. and C. Technology, undefined 2019, Cored-wire arc spray fabrication of novel aluminium-copper coatings for anti-corrosion/fouling hybrid performances, Elsevier.
- [91] Devaraj S, Anand B, Gibbons M, McDonald A, Chandra S. Thermal spray deposition of aluminum and zinc coatings on thermoplastics. *Surface and Coatings Technology*. 2020 Oct 15;399:126114. [92] A. Rezzoug, S. Abdi, A. Kaci, M.Y.-S. and C. Technology, 2018, Thermal spray metallisation of carbon fibre reinforced polymer composites: Effect of top surface modification on coating adhesion and mechanical properties, Elsevier.
- [93] S. Nigam, S. Mahapatra, S.P.-S. Engineering, 2019, Effect of stand-off distance in thermally sprayed copper coating, *Taylor & Francis*. 35 (2019) 826–832.
- [94] R. Kromer, S. Costil, C. Verdy, S. Gojon, H.L.C. Technology, 2018, Laser surface texturing to enhance adhesion bond strength of spray coatings—Cold spraying, wire-arc spraying, and atmospheric plasma spraying, Elsevier.

- [95] A. Liu, M. Guo, M. Zhao, H. Ma, S.H.-S. and C. Technology, 2006, Arc sprayed erosion-resistant coating for carbon fiber reinforced polymer matrix composite substrates, Elsevier.
- [96] S. Devaraj, B. Anand, M. Gibbons, A. McDonald, S. Chandra, Thermal spray deposition of aluminum and zinc coatings on thermoplastics, *Surface and Coatings Technology*. 399 (2020) 126114.
- [97] V. Rat, F. Mavier, J.F. Coudert, Electric Arc Fluctuations in DC Plasma Spray Torch, *Plasma Chemistry and Plasma Processing*. 37 (2017) 549–580.
- [98] C. Chazelas, J.P. Trelles, A. Vardelle, The Main Issues to Address in Modeling Plasma Spray Torch Operation, *Journal of Thermal Spray Technology*. 26 (2017) 3–11.
- [99] F. Mavier, F. Zoubian, V.R.P.D.A. Physics, 2018, Electric arc in a plasma spray torch under modulated current, *Iopscience.Iop.Org*. 51 (2018) 405201.
- [100] Y. Kawaguchi, F. Miyazaki, M. Yamasaki, Y. Yamagata, N. Kobayashi, K. Muraoka, Coating qualities deposited using three different thermal spray technologies in relation with temperatures and velocities of spray droplets, *Mdpi.Com*. (2017).
- [101] J. Odhiambo, W. Li, Y. Zhao, C.L.- Coatings, undefined 2019, Porosity and its significance in plasma-sprayed coatings, *Mdpi.Com*.
- [102] N. Curry, M. Leitner, K.K.- Coatings, 2020, High-porosity thermal barrier coatings from high-power plasma spray equipment—processing, performance and economics, *Mdpi.Com*.
- [103] L. Kinner, E. List-Kratochvil, T.D.- Nanotechnology, 2020, Gentle plasma process for embedded silver-nanowire flexible transparent electrodes on temperature-sensitive polymer substrates, *Iopscience.Iop.Org*. (2020).
- [104] L. Łatka, L. Pawłowski, M. Winnicki, P. Sokołowski, A. Małachowska, S. Kozerski, Review of functionally graded thermal sprayed coatings, *Mdpi.Com*.
- [105] M. Aghasibeig, F. Tarasi, R.S. Lima, A. Dolatabadi, C. Moreau, A Review on Suspension Thermal Spray Patented Technology Evolution, *Journal of Thermal Spray Technology*. 28 (2019) 1579–1605.
- [106] A. Rezzoug, S. Abdi, A. Kaci, M. Yandouzi, Thermal spray metallisation of carbon fibre reinforced polymer composites: Effect of top surface modification on coating adhesion and mechanical properties, *Surface and Coatings Technology*. 333 (2018) 13–23.
- [107] W. Huang, X. Gan, L. Zhu, Fabrication and property of novel double-layer coating deposited on polyimide matrix composites by atmospheric plasma spraying, *Ceramics International*. 44 (2018) 5473–5485.
- [108] S. Yan, X. Zhou, H. Zhang, S. Dong, X. Li, J. Jiang, X. Cao, Correction to: HVOF-Sprayed AlSi50 Alloy Coatings as a Novel Electrothermal Anti-icing/De-icing System for Polymer-based Composite Structures, *Journal of Thermal Spray Technology* 2021 31:3. 31 (2021) 658–658.

- [109] H. Che, A. Liberati, X. Chu, M. Chen, A.N.-... C. Technology, 2021, Metallization of polymers by cold spraying with low melting point powders, Elsevier.
- [110] H. Che, P. Vo, S. Yue, Metallization of carbon fiber reinforced polymers by cold spray, *Surface and Coatings Technology*. 313 (2017) 236–247.
- [111] J. Sun, K. Yamanaka, S. Zhou, H. Saito, Y. Ichikawa, K. Ogawa, A. Chiba, Adhesion mechanism of cold-sprayed Sn coatings on carbon fiber reinforced plastics, *Applied Surface Science*. 579 (2022) 151873.
- [112] J. Sun, S. Zhou, K. Yamanaka, Y. Ichikawa, H. Saito, K. Ogawa, A. Chiba, Thermal Effects in Sn Coating on a Carbon Fiber Reinforced Plastic by Cold Spraying, *Journal of Thermal Spray Technology*. 30 (2021) 1254–1261.
- [113] A.V. Walker, *Metalization of Functionalized Surfaces*.
- [114] A.M. Tarditi, M.L. Bosko, L.M. Cornaglia, 3.1 Electroless.
- [115] M.A. Azmah Hanim, 3.15 Electroless Plating as Surface.
- [116] A. Islam, H. Hansen, P.T.-C. Annals, 2017, Direct electroplating of plastic for advanced electrical applications, Elsevier.
- [117] H. Wu, Y. Huang, M. Zong, J. Shao, W. Zhang, Effect of surface preparation on electroless Ni-P plating on carbon fiber-Reinforced Cyanate Ester Resin Laminate, *Wiley Online Library*. 37 (2016) 1161–1166.
- [118] P.S.M. Rajesh, X. Cauchy, M. Gagne, J.E. Klemberg-Sapieha, F. Sirois, D. Therriault, Wet chemical metallization of aerospace composites as a lightning protection strategy, *Engineering Solutions for Sustainability: Materials and Resources II*. (2016) 187–192.
- [119] S. Jiang, R.G.-S. modification of textiles, 2009, *Modification of textile surfaces using electroless deposition*, Elsevier.
- [120] M. Benelmekki, A.E.-F. of Nanoscience, 2019, Nanostructured thin films—background, preparation and relation to the technological revolution of the 21st century, Elsevier.
- [121] A. Behera, P. Mallick, S.M.-C.P. at the Nanoscale, undefined 2020, *Nanocoatings for anticorrosion: An introduction*, Elsevier.
- [122] A. Rockett, *The materials science of semiconductors*, 2007.
- [123] *Metallization of carbon fiber reinforced polymers: Chemical kinetics, adhesion, and properties*, Elsevier.
- [124] F. Addou, T. Duguet, Y. Ledru, D. Mesnier, C.V.- *Coatings*, 2021, Engineering Copper Adhesion on Poly-Epoxy Surfaces Allows One-Pot Metallization of Polymer Composite Telecommunication Waveguides, *Mdpi.Com*.

- [125] T. Duguet, F. Senocq, L. Laffont, C.V.C. Technology, undefined 2013, Metallization of polymer composites by metalorganic chemical vapor deposition of Cu: Surface functionalization driven films characteristics, Elsevier.
- [126] Z. Guo, L. Sang, Z. Wang, Q. Chen, L.Y.-... and C. Technology, 2016, Deposition of copper thin films by plasma enhanced pulsed chemical vapor deposition for metallization of carbon fiber reinforced plastics, Elsevier.
- [127] B. Fotovvati, N. Namdari, A. Dehghanghadikolaei, On coating techniques for surface protection: A review, Mdpi.Com.
- [128] A.M.-N. and ultra-thin films, undefined 2011, Current and advanced coating technologies for industrial applications, Elsevier.
- [129] B. Coto, P. Hallander, L. Mendizabal, F. Pagano, H.K.- Wear, undefined 2021, Particle and rain erosion mechanisms on Ti/TiN multilayer PVD coatings for carbon fibre reinforced polymer substrates protection, Elsevier.
- [130] D.M. Devine, J. Hahn, R.G. Richards, H. Gruner, R. Wieling, S.G. Pearce, Coating of carbon fiber-reinforced polyetheretherketone implants with titanium to improve bone apposition, Wiley Online Library. 101 (2012) 591–598.
- [131] C. Maurer, U.S.- Wear, undefined 2013, Erosion resistant titanium based PVD coatings on CFRP, Elsevier.
- [132] C. Maurer, U.S.- Wear, undefined 2014, Solid particle erosion of thick PVD coatings on CFRP, Elsevier.
- [133] G. Vergason, M. Fitch, R. Smith, M.B.-Soc.Vac. Coaters, 2015, PVD chromium coatings replacing decorative chromium electroplated coatings on plastics, Vergason.Com.
- [134] J.W.-S. and C. Technology, 1988, Grit blasting as surface preparation before plasma spraying, Elsevier.
- [135] D.V. Jr, L. Lundberg, R. Hartley, Surface preparation via grit-blasting for thermal spraying, (1995).
- [136] J. Day, X. Huang, N.R.-J. of T.S. Technology, undefined 2005, Examination of a grit-blasting process for thermal spraying using statistical methods, Springer. 14 (2005) 471–479.
- [137] L.W. McKeen, Substrates and Substrate Preparation, Fluorinated Coatings and Finishes Handbook. (2016) 129–146.
- [138] Z. Yu, H.I. Lin, Development of robotic polishing/fettling system on ceramic pots.
- [139] A. di Gianfrancesco, Technologies for chemical analyses, microstructural and inspection investigations, Materials for Ultra-Supercritical and Advanced Ultra-Supercritical Power Plants. (2017) 197–245.

